Science of the Total Environment 829 (2022) 154669

Contents lists available at ScienceDirect

Science of the Total Environment

journal homepage: www.elsevier.com/locate/scitotenv

# Modeling the impacts of land use/land cover change on meteorology and air quality during 2000–2018 in the Yangtze River Delta region, China

Li Li [a,b], Ansheng Zhu [a,b], Ling Huang [a,b], Qing Wang [c], Yixiao Chen [d], Maggie Chel Gee Ooi [e], Min Wang [c], Yangjun Wang [a,b,*], Andy Chan [d,**]

[a] School of Environmental and Chemical Engineering, Shanghai University, Shanghai 200444, China
[b] Key Laboratory of Organic Compound Pollution Control Engineering (MOE), Shanghai University, Shanghai 200444, China
[c] Shanghai Academy of Environmental Sciences, Shanghai 200233, China
[d] Department of Civil Engineering, University of Nottingham Malaysia, Semenyih 43500, Selangor, Malaysia
[e] Institute of Climate Change (IPI), National University of Malaysia (UKM), 43600 Bangi, Selangor, Malaysia

## HIGHLIGHTS

- Rapid urbanization and decrease in croplands are the main characterizations of LULC change over the YRD region from 2000 to 2018.
- Rapid urbanization leads to an increase of monthly mean 2-m temperature by 0.4–2.1 °C but decrease of the 10-m wind speed by 0.5–1.3 m/s in urban areas.
- Surface $O_3$ concentration in urban areas has increased while $PM_{2.5}$ decreased due to LULC changes in the past two decades.

## GRAPHICAL ABSTRACT

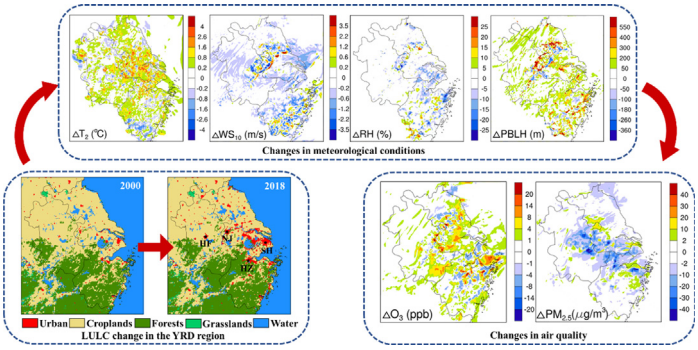


## ARTICLE INFO

*Article history:*
Received 21 January 2022
Received in revised form 8 March 2022
Accepted 15 March 2022
Available online 18 March 2022

Editor: Jianmin Chen

*Keywords:*
LULC change
Meteorology
Air quality
Yangtze River Delta

## ABSTRACT

The land use/land cover (LULC) change in the fast-developing city clusters of China exhibits impacts on both the meteorology and air quality. However, this effect, especially in the Yangtze River Delta (YRD), has not been well quantified. In this study, the LULC data are extracted from Landsat satellite imageries for year 2000 and 2018 for the YRD region. The Weather Research and Forecasting with Chemistry (WRF/Chem) model is applied to investigate the impact of historical LULC change on regional meteorology and air pollution over the YRD region during the past two decades. Two simulation scenarios are performed with two sets of LULC data to represent the pre-urbanization (LULC of year 2000) and the most recent urban pattern (LULC of year 2018). Results indicate that rapid urbanization leads to an increase of monthly mean 2-m temperature by 0.4–2.1 °C but decrease of the 10-m wind speed by 0.5–1.3 m/s in urban areas; the maximum increase of daytime planetary boundary layer height (PBLH) in July and November is 289 and 132 m, respectively. Affected by favorable changes in the meteorological conditions due to LULC change, the $PM_{2.5}$ concentrations in most urban areas show a decreasing trend, especially during the nighttime in summer. On the contrary, surface ozone ($O_3$) concentration in urban areas has increased by 7.2–9.8 ppb in summer and 1.9–2.1 ppb in winter. Changes in $O_3$ concentration are inversely proportional to changes in $NO_x$ and the spatial distribution of $PM_{2.5}$. Areas with higher $O_3$ concentration are consistent with areas of higher temperature and lower wind speed. Our findings reveal that LULC changes during the past years bring observable changes in air pollutant concentrations, which should not be neglected in the YRD region regarding air quality trends as well as policy evaluations under the warming threat.

* Correspondence to: Y. Wan, School of Environmental and Chemical Engineering, Shanghai University, Shanghai 200444, China.
** Corresponding author.
*E-mail addresses:* yjwang326@shu.edu.cn (Y. Wang), Andy.Chan@nottingham.edu.my (A. Chan).

http://dx.doi.org/10.1016/j.scitotenv.2022.154669

## 1. Introduction

Changes of land use/land cover (LULC) exhibit significant impacts on the environment (Seto and Shepherd, 2009). In recent years, LULC has changed rapidly in developing countries, particularly in China (Deng et al., 2020; Güneralp et al., 2015; Li and Li, 2019) due to fast social and economic development (Dewan et al., 2012; Seto et al., 2002; Verburg et al., 2004). Xu et al. (2014) identified the saturation of nighttime light brightness in the urban center and found significant increases in suburban region of China from 1992 to 2009. With the aid of the impervious surface as an indicator, Gong et al. (2019) reported that the area of Chinese cities and towns in 2017 was 13.6 times of that in 1978. Land use types, such as cultivated land, woodland, and grassland have been transformed into urban construction land as a result of urban expansion in the past decade (El-Hamid et al., 2021; Sati and Mohan, 2018). These changes not only affect the thermal and physical properties of the land surfaces including roughness, thermal inertia, and albedo (Ghimire et al., 2014; Sun et al., 2012) but also generate new dynamical and thermodynamic processes (Cheng and Byun, 2008; Kaplan et al., 2017). In addition, the impact of LULC on regional climate affects the transport and diffusion of air pollutants in the atmosphere (Zheng et al., 2017).

The spatial pattern of air quality parameters in urban areas is often closely related to the level of urbanization (Ku, 2020). Urbanization due to population growth and increased economic activities results in massive emissions of air pollutants, thereby exacerbating the air quality (Cole and Neumayer, 2004; Fang et al., 2015). Ozone ($O_3$) is an important secondary pollutant in the atmosphere and is influenced by the changes in meteorological conditions due to LULC. Ryu et al. (2013) demonstrated that the surface $O_3$ concentration is 16 ppb higher at nighttime and 13 ppb higher at daytime due to urbanization in the Seoul metropolitan area. According to Chen et al. (2018), conversion of rural to urban land surfaces in Beijing increased surface air temperature and planetary boundary layer height (PBLH), resulting in a rise in surface $O_3$ concentrations by 9.5 ppb.

The YRD region is one of the largest urban agglomerations in China, located in the north marine monsoon subtropical climate zone of southeast China. This region has experienced unprecedented economic development and drastic urbanization in the past three decades (Gu et al., 2011; Han et al., 2017). Air pollution has been largely aggravated as a result of meteorological environment and anthropogenic emissions (Li et al., 2019a; Li et al., 2018; Li et al., 2019b). Different from the urban agglomeration in North China like the Beijing-Tianjin-Hebei (BTH) region where it is a semi-humid continental monsoon climate with four distinct seasons (Zhao et al., 2013), the YRD region is dominated by a humid climate with mild winter and hot, muggy summer (Zhang et al., 2015). Therefore, the impacts of LULC change in YRD region on air quality are expected to be different from other regions. For example, the reduction of daytime radiation intensity during winter in BTH region due to urbanization led to a reduction of $O_3$ concentration (Tao et al., 2018), while urban sprawl in YRD region caused noticeable increases in daytime $O_3$ concentration (Liao et al., 2015). Wang et al. (2009a) also reported similar results that LULC change from the early 1990s to 2001 enhanced the surface $O_3$ level by about 4.7% during nighttime and 2.9% during daytime over the Pearl River Delta (PRD) and YRD regions, two highly urbanized regions in China. With the dominant ongoing changes in LULC being urbanization, Zhan and Xie (2022) found that changes in surface temperature, wind speed, and PBLH lead to increase in $O_3$ concentration by a maximum of 20 $\mu g/m^3$ in Shanghai due to urban sprawl. Additionally, the spatial distributions of ambient fine particulate matter ($PM_{2.5}$) present large regional variations among BTH, PRD, and YRD, which is highly correlated with land use type (Zhang et al., 2019). Remarkable differences in the relationship between urban form and $PM_{2.5}$ concentration exist in different urban agglomerations (Mao et al., 2022).

Previous studies have primarily focused on cities in developed countries or only a specific megacity whereas developing countries suffer much more serious air pollution due to fast urbanization. In addition, changes in other land use types may also significantly affect the surface properties and further influence the regional meteorological conditions and air quality. In a rapid economic development area like YRD region, LULC alters noticeably in a relatively short period and it is necessary to evaluate the consequences of LULC changes. Therefore, to fill the gap described above, we systematically investigate the impacts of LULC change on meteorology and regional air quality in YRD region for the past two decades. Results of this study can provide guidance to future urban planning as well as air pollution projection and control.

## 2. Methodologies

### 2.1. Land use/land cover data interpretation

In this study, to better characterize the real land surface of the YRD region, LULC data are extracted from Landsat-5/7/8 imageries acquired from United States Geological Survey (USGS) official website. Using Geographic Information System (GIS), land use maps for year 2000 (LULC_2000) and year 2018 (LULC_2018) are reprojected into WRF-identifiable WGS84 (World Geodetic System 1984) ellipsoids. According to the International Geosphere Biosphere Programme (IGBP) land classification, the original data are reclassified for the same 20 land use categories as MODIS-IGBP with a horizontal resolution of 1 km (Table S1). Fig. S1 shows the technical flowchart of land use data conversion.

### 2.2. Model configuration

The WRF/Chem v3.9 (Grell et al., 2005) model is applied to simulate meteorological fields and air quality fields. In this study, three nested domains are used: horizontal grid resolution for domain 1 (D01), 2 (D02), and 3 (D03) are 36 km, 12 km, and 4 km, respectively, and 24 sigma levels with a model top set at 100 hPa are used, the first 19 layers are within the planetary boundary layer. The D01 covers most of East Asia and part of Southeast Asia; D02 covers east China and D03 encompasses the entire YRD region (Fig. 1a). The YRD region comprises Shanghai (SH) and Jiangsu, Zhejiang, and Anhui provinces, with provincial capitals of Nanjing (NJ), Hangzhou (HZ), and Hefei (HF), respectively. Fig. 1b illustrates the terrain and meteorology for the study region, as well as the locations of observation stations. The meteorological initial and boundary conditions of the model are 6 hourly (1.0° × 1.0° resolution) Global Final Analysis (FNL) data, provided by the National Center for Environmental Prediction-National Center for Atmospheric Research (NCEP/NCAR). The chemical initial fields are provided with outputs from the previous model cycle. The anthropogenic emission inventory used in this study is from the China Multi-scale Emission Inventory (MEIC) with 0.25° × 0.25° resolution developed by Tsinghua University (Zheng et al., 2018), which consists of provincial data from five sectors (power, agriculture, residential, industry, and transportation) (http://meicmodel.org/). The biogenic emissions are calculated by the Model of Emissions of Gases and Aerosol from Nature (MEGAN) (Guenther et al., 2006), which is online coupled in the WRF/Chem model. The physical options contain the Lin microphysics scheme (Lin et al., 1983), the NOAH land surface scheme (Chen and Dudhia, 2001), the Kain-Fritsch (KF) cumulus parameterization (only used in D01 and D02) (Kain and Fritsch, 1993), the Rapid Radiative Transfer Model shortwave radiation scheme and the Rapid Radiative Transfer Model longwave radiation scheme (Mlawer et al., 1997), and the YSU boundary layer scheme (Hong et al., 2006).The gas phase chemistry mechanism is the Regional Acid Deposition Model-2nd generation (RADM2) (Stockwell et al., 1990) chemical mechanism, including 63 chemical species and 136 gas phase reactions. The aerosol module is the Modal Aerosol Dynamics Model for Europe-Secondary Organic Aerosol Model (MADE-SORGAM) (Schell et al., 2001). The physical and chemical schemes used in this study are listed in Table S2.

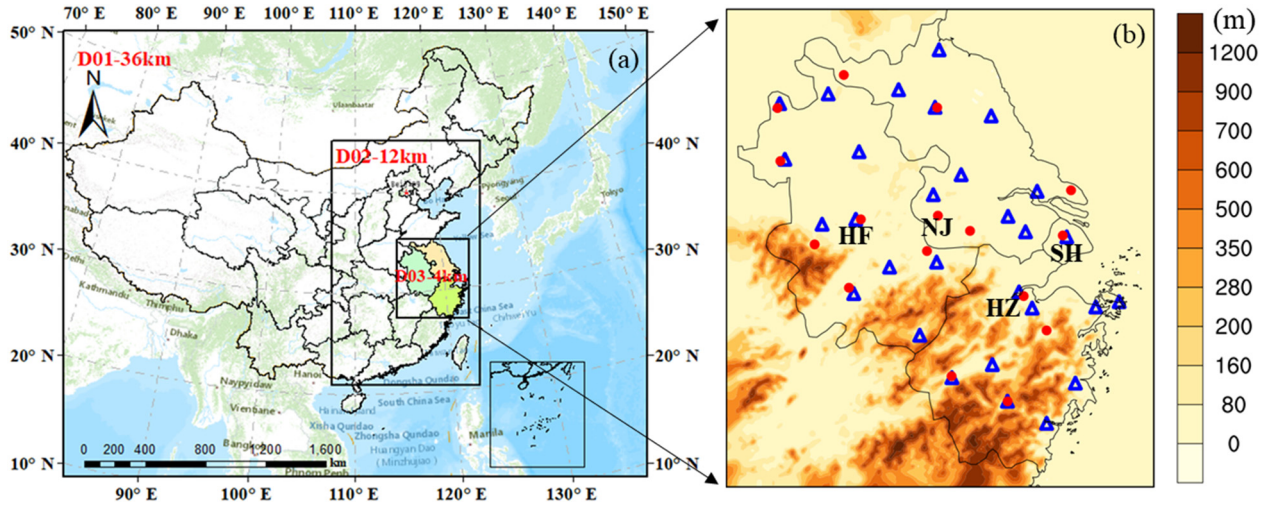


**Fig. 1.** The three nested modeling domains for model simulation (a); terrain height for the YRD region and distribution of ground observational stations (red dots and blue triangles are meteorological and air quality observation sites, respectively) (b).

### 2.3. Design of simulation scenarios

This study mainly focusses on the direct influence of LULC change on meteorology and indirect influence on chemistry through the changes of physical aspects caused by land use change. We do not look at the direct influence of land use change on chemistry (or anthropogenic emission aspect). Therefore, two different scenarios are simulated to investigate the impact of LULC change in the YRD area. LULC_2000 scenario represents land use pattern of YRD region in 2000, while LULC_2018 scenario depicts land use pattern of YRD region in 2018. The biogenic emission changes are not fixed but changes with the land use changes, and are calculated based on MEGAN coupled within the WRF/Chem model. Simulation is performed for July and November in 2018, representing summer and winter respectively. The model is run as a series of smaller simulations of 144 h (six days) duration with 24 h overlap between every two consecutive runs to improve the model performance. The first 24 h are considered as model spin up and the rest 120 h are used for analysis from each of the five-day simulations. The same physics schemes, dynamics configurations, and emission inventory are applied for both cases except for static data (LULC datasets). Two scenarios are analyzed: the Base Scenario (LULC_2018) as control case, using 2018 LULC of YRD; the Comparison Scenario (LULC_2000) in which the 2000 LULC is used (Table 1).

## 3. Results and discussions

### 3.1. Model performance evaluation

#### 3.1.1. Meteorology

We used statistical indices including the mean bias (MB), the mean square error (RMSE), correlation coefficients (R), normalized mean bias (NMB), normalized mean error (NME), mean fractional error (MFE) and the mean fractional bias (MFB) to evaluate the model performance. Descriptions of the statistical indices are described in the Supporting Information. The 2-m temperature ($T_2$) and 10-m wind speed ($WS_{10}$) for the base scenario (LULC_2018) are compared with the hourly observations of ground meteorological stations obtained from the National Oceanic and Atmospheric Administration (NOAA)'s Climate Data Center archive (http://www.ncdc.noaa.gov/oa/ncdc.html). As shown in Fig. S2, simulated meteorological variables well match the actual temperature and wind speed changes for July and November. Table 2 presents the statistical metrics for meteorological factors, which are described in the Supporting Information. The simulations of $T_2$ show the highest correlation coefficients (R) for both July and November of 0.88 and 0.94, manifesting that the simulations generally reflect the characteristics of $T_2$. For wind speed, the RMSE of July is higher than November (1.1 for July and 0.9 for November) and R of July is lower than November (0.70 for July and 0.79 for November). It is due to strong turbulent mixing and unstable atmospheric layer developed in summer (Pan and Gu, 2016; Prasad et al., 2017). Emery et al. (2001) proposed benchmarks for validation of simulated temperature (MB within ±0.5 °C) and wind speed (MB within ±0.5 m/s and RMSE <2 m/s). Based on their results, the meteorological performances in our study meet the proposed criteria (Table 2). In general, simulated meteorological factors are in good agreement with the observations.

**Table 1**
Description of numerical simulation scenarios.

| Scenario definition | Abbreviation | Land use data | Meteorology data | Anthropogenic emission |
|---|---|---|---|---|
| Base Scenario | LULC_2018 | 2018 | FNL_2018 | MEIC_2018 |
| Comparison Scenario | LULC_2000 | 2000 | FNL_2018 | MEIC_2018 |

#### 3.1.2. Air quality

Hourly time series of $PM_{2.5}$ and $O_3$ concentrations collected at 29 air quality monitoring stations acquired from national real-time release platform for urban air quality of China National Environmental Monitoring Centre (http:// air.cnemc.cn:18007) are compared with simulations to evaluate the model performance of chemical fields. Time-series comparisons are shown in Fig. S3 and statistics are presented in Table 3. The base scenario simulation exhibit that the WRF/Chem model generally predicts the changes in $PM_{2.5}$ and $O_3$ concentration distributions in July and November. Monthly mean simulated $PM_{2.5}$ and $O_3$ concentrations are 23.2 ± 9.8 μg/m$^3$ and 36.6 ± 18.8 ppb; 42.8 ± 16.7 μg/m$^3$ and 27.5 ± 8.2 ppb in July and November, respectively. The corresponding observations are 22.9 ± 6.2 μg/m$^3$ and 34.6 ± 19.7 ppb; 43.5 ± 17.2 μg/m$^3$ and 20.8 ± 15.4 ppb in July and November, respectively. It is suggested that the model performance criteria for air pollutants is met when both the MFE and the MFB are less than or equal to approximately +75% and ± 60%, respectively (Boylan and Russell, 2006; Epa, 2007). The results shown in Table 3 indicate that the performances of air quality simulation for $PM_{2.5}$ and $O_3$ are acceptable. For $PM_{2.5}$, the model performances also successfully meet the benchmarks proposed for China by Huang et al. (2021). The $PM_{2.5}$ concentrations show slight overestimation in July and

**Table 2**
Model performance statistics for meteorological simulation of LULC_2018.

| Variables | July | | | | | November | | | | |
|---|---|---|---|---|---|---|---|---|---|---|
| | MS ± Std[a] | MO ± Std[a] | MB | RMSE | R | MS ± Std | MO ± Std | MB | RMSE | R |
| $T_2$(°C) | 30.0 ± 2.7 | 29.7 ± 2.8 | 0.3 | 1.4 | 0.88 | 14.3 ± 2.2 | 13.8 ± 2.5 | 0.5 | 1.2 | 0.94 |
| $WS_{10}$(m/s) | 3.7 ± 1.4 | 3.2 ± 1.2 | 0.5 | 1.1 | 0.70 | 3.0 ± 1.1 | 2.5 ± 1.0 | 0.5 | 0.9 | 0.73 |
| RH(%) | 72.1 ± 14.1 | 81.3 ± 14.5 | −5.35 | 12.58 | 0.64 | 73.5 ± 13.6 | 81.4 ± 14.6 | −5.48 | 13.05 | 0.69 |

[a] MS and MO represent the mean simulations and observations, respectively.

**Table 3**
Model performance statistics for air quality simulation of LULC_2018.

| Variables | July | | | | | November | | | | |
|---|---|---|---|---|---|---|---|---|---|---|
| | NMB | NME | MFB | MFE | R | NMB | NME | MFB | MFE | R |
| $PM_{2.5}$(μg/m$^3$) | 0.7 | 32.3 | −3.7 | 31.9 | 0.47 | −0.8 | 34.5 | 0.9 | 35.2 | 0.51 |
| $O_3$(ppb) | 3.6 | 25.0 | 7.9 | 28.9 | 0.83 | 33.6 | 46.3 | 46.4 | 57.4 | 0.75 |

underestimation in November, with the NMB of 0.7% and − 0.8%, respectively. Underestimation of $PM_{2.5}$ concentration is in part attributed to the positive bias of temperature in November, deeper boundary layer is formed and $PM_{2.5}$ is well-mixed within the boundary layer (Miao et al., 2019). The magnitudes trends for $O_3$ concentrations are reasonably predicted in July, with an overall correlation coefficient of 0.83 and NMB of 3.6%. The NME for $O_3$ is larger in November (46.3%) than in July (25.0%). The above demonstrates that the simulated errors are acceptable and simulations can capture the characteristics of chemical fields.

### 3.2. LULC change from 2000 to 2018

Fig. 2 shows that the YRD region experienced significant LULC changes from 2000 to 2018. Urban and built-up land area has increased from 36,326 km$^2$ to 54,610 km$^2$, with a growth rate of 50.3% (Table S3). The rapidly urbanized areas are centralized not only in provincial cities like SH, HZ, NJ, and HF, but in the lines including Shanghai-Wuxi-Suzhou-Nanjing belt, Hangzhou-Jiaxing-Huzhou-Shanghai belt as well as coastal cities like Ningbo. In addition, the decrease in croplands is prominent. As the most dominant LULC type, croplands occupy more than 40% of the whole YRD area. They are mainly distributed in the northern regions of the study area. The reduction of croplands is 18,522 km$^2$ and most of them have transformed to urban and built-up land. Forests are mainly distributed in the southern area of the YRD region, and its area is second to croplands. Changes in forest are negligible, with a growth rate of only 0.7%. Grassland has decreased from 4998 km$^2$ to 3945 km$^2$.

### 3.3. Impacts of LULC change on meteorology

#### 3.3.1. 2-m temperature

The changes of LULC over the YRD region leads to changes of land surface properties such as emissivity, heat capacity, and soil temperature, which consequently affect surface air temperature. Fig. 3 shows the spatial difference of average monthly $T_2$ between LULC_2018 and LULC_2000 scenarios (i.e., LULC_2018 minus LULC_2000) at 14 Local Standard Time (LST) for daytime and 20 LST for nighttime in July and November 2018 for the YRD region, respectively. After updating the LULC data, $T_2$ exhibits varying degrees of spatial, seasonal, and daily changes over YRD region. The patterns of $T_2$ positive differences are similar to the urbanization region,

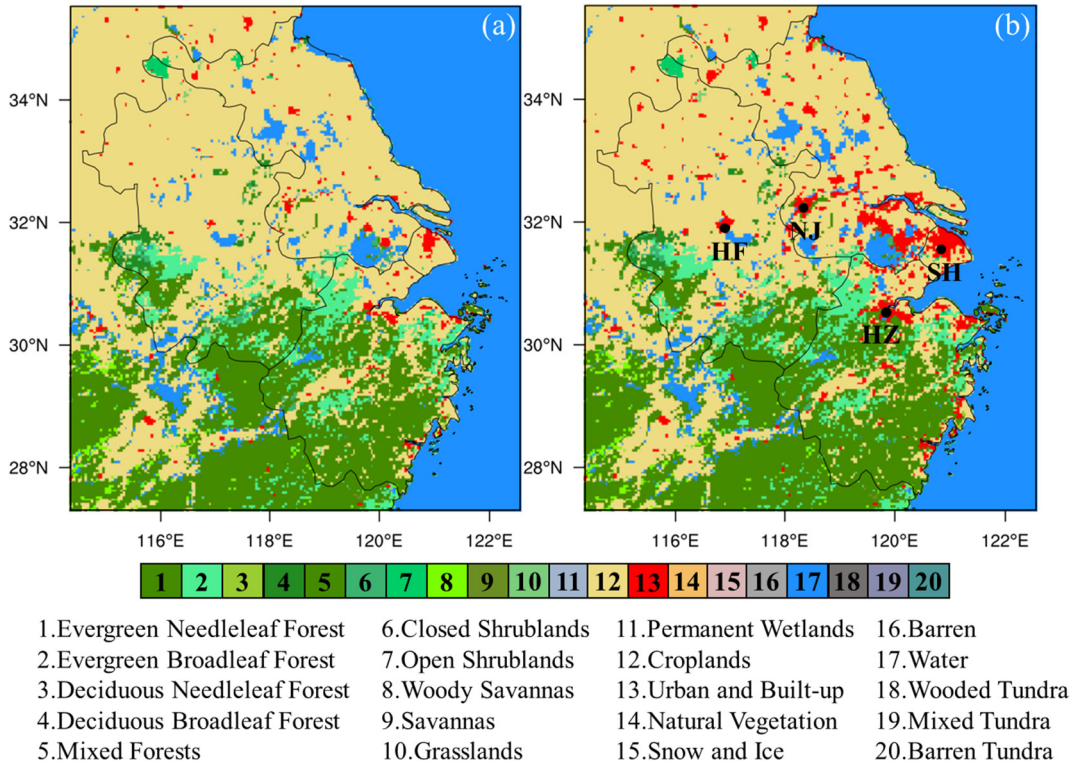


**Fig. 2.** LULC data over the YRD region derived from satellite imageries in 2000 (a) and 2018 (b), respectively.

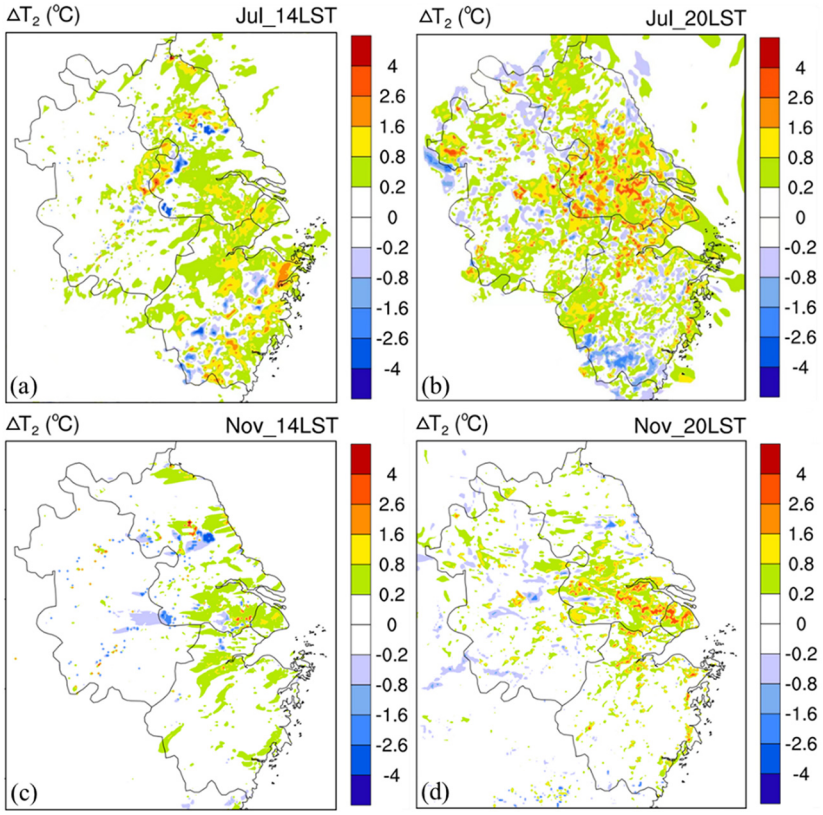


**Fig. 3.** Spatial distribution of monthly average $T_2$ differences between LULC_2018 and LULC_2000 for July_14LST(a), July_20LST(b), November_14LST (c) and November_20LST(d).

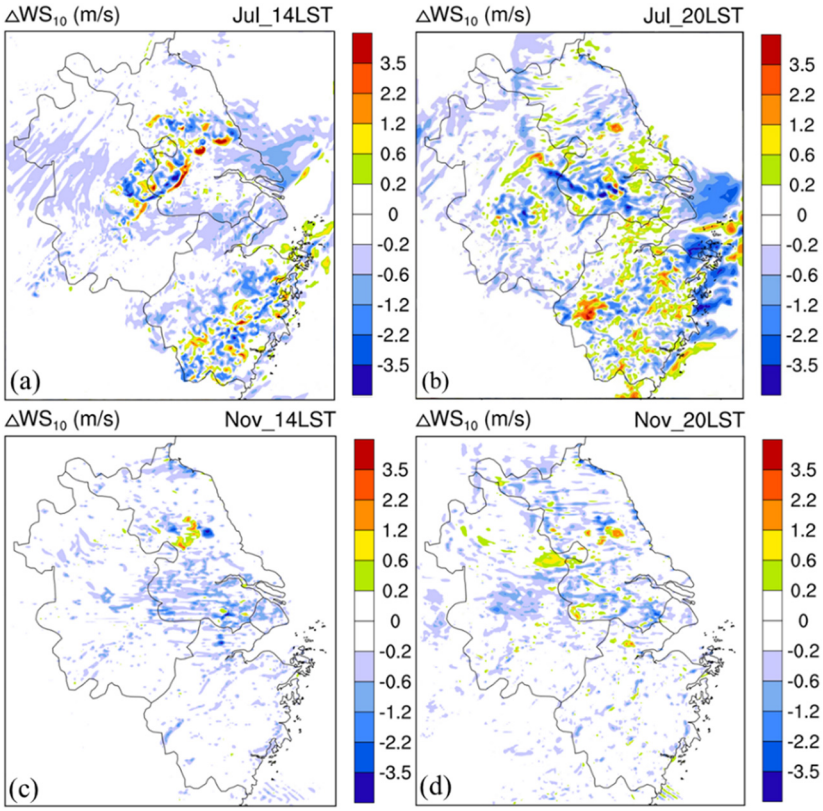


**Fig. 4.** Spatial distribution of monthly average $WS_{10}$ differences between LULC_2018 and LULC_2000 for July_14LST(a), July_20LST(b), November_14LST(c) and November_20LST(d).

ranging from 0.2–1.6 ˚C. Remarkably, the higher $T_2$ difference occurs around the urban areas. $T_2$ in urban-grid during July (November) increased by an average of 1.5 ˚C (0.4 ˚C) for daytime and 2.1 ˚C (1.2 ˚C) for nighttime. Results show that the rise of $T_2$ is more evident at nighttime. This may be attributed to the conversion of other land use types to urban, which changes the surface albedo and affect the absorption of solar radiation by altering the urban land surface (Trlica et al., 2017; Vahmani et al., 2016). During the day, the urban structure absorbs and stores more radiation, while the heat flux released by the urban canopy is larger, resulting in the increase of surface temperature at nighttime (Du et al., 2007; Lin et al., 2009). Furthermore, seasonal variations are observed with larger increase of $T_2$ simulated in July than that in November. In winter, the warming effect due to urbanization is mainly concentrated in urban areas of the mid-eastern part of YRD region, especially at night. In summer, in addition to the central and eastern areas, warming effect also appears in the southern part of YRD region.

*3.3.2. 10-m wind speed*

After updating the LULC, rapid urbanization also increases the surface roughness, which exerts a drag on the airflow in the canopy and affects the surface wind speed and mass transport in the atmosphere. Fig. 4 shows that overall, the 10-m wind speed ($WS_{10}$) decreases in both summer and winter. The variation of $WS_{10}$ demonstrates regional characteristics that in high-density urban areas, the decrease of $WS_{10}$ could reach 2.2 m/s at nighttime in summer. It should also be noticed that the increase of wind speed is quite substantial in several regions surrounding the city centers especially in summer nighttime. The reason is probably that the local circulation effect caused by the stronger heat island effect due to the weaker suburban wind speed and stable atmosphere causes the increase in wind speed at nighttime. In some hilly regions, wind speed increases as well, which will be discussed in Section 3.5. In addition, the difference of $WS_{10}$ also reflects temporal variability that decrease of $WS_{10}$ in urban region is larger in summer than winter, with magnitude of 1.3 m/s at 14LST, 1.1 m/s at 20 LST in July and 0.7 m/s at 14 LST, 0.5 m/s at 20 LST in November, respectively. Except for east-central urban areas in YRD region, cities far from the coastal zone also display more noticeable weakening of $WS_{10}$ in summer than in winter.

*3.3.3. Relative humidity*

The increase in $T_2$ and lesser evaporation of water due to land use change decrease the near surface relative humidity (RH) (Fig. 5). Seasonally, reduction of RH in July is larger than in November. Decreases in monthly mean RH over urban areas are 12%–19% during summer and 6%–9% in winter. Rising $T_2$ causes more water vapor to evaporate. On the other hand, natural land surfaces including grasslands, croplands, and woodlands are transformed into impervious urban surface in urban dominated by cement, which cause a reduction in surface moisture and result in the decrease in RH. Abundant water vapor and higher surface

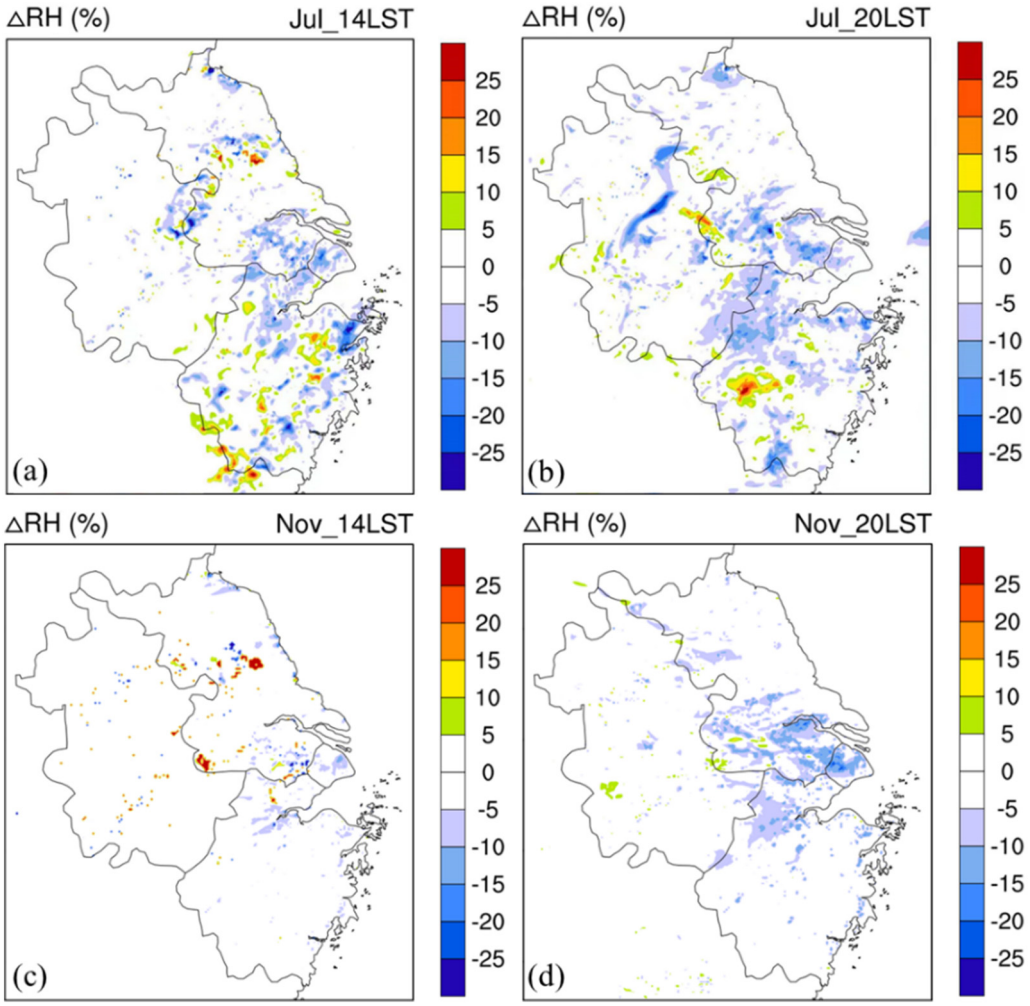


**Fig. 5.** Spatial distribution of monthly average RH differences between LULC_2018 and LULC_2000 for July_14LST(a), July_20LST(b), November_14LST(c) and November_20LST(d).

temperature in summer are the main reasons for the greater variations of RH than in winter. Wang et al. (2014) also found that the effects of urbanization on RH are greater in summer than in winter.

#### 3.3.4. Planetary boundary layer height

PBLH is a meteorological variable that affects the mixed exchange of surface water vapor, heat, and upper-level momentum, making it a key parameter in modeling vertical mixing and dilution of near-surface pollutants (Ayotte et al., 1996; Haeffelin et al., 2012; Jia and Zhang, 2020). In this study, the changes of PBLH (Fig. 6) are similar to the spatial distributions of $T_2$ in both summer and winter, showing an overall increasing trend especially in urban areas. Larger differences at 14 LST and lower differences at 20 LST due to the variation of $T_2$ and sensible heat flux (Fig. S4) are observed in July and November. The increase of PBLH in summer is greater compared to winter, with maximum value of 560 m and 320 m at 14 LST in July and November respectively. Furthermore, PBLH increases significantly during daytime over urban areas. During daytime, the average increase of PBLH in urban areas is 289 m (~41%) in July and 82 m (~17%) in November. During nighttime, the increase of PBLH is 132 m (~82%) in July and 45 m (~35%) in November. In summer, PBLH changes more conspicuously due to the unstable atmosphere. In general, the rise of PBLH in urban areas is mainly attributed to the increased storage of heat.

### 3.4. Impacts of LULC change on air quality

#### 3.4.1. $PM_{2.5}$ concentration

Meteorological parameters affected by changes of LULC will further exert an influence on air quality through formation, horizontal transportation, and vertical diffusion of air pollutants. In this study, $PM_{2.5}$ is chosen as the indicator to investigate the influence of urbanization on particulate matter pollution. With changes of LULC, domain-wide $PM_{2.5}$ concentration decreases in July and November, with urban regions being mostly affected (Fig. 7). It is worth noting that there is a small area where $PM_{2.5}$ concentration increases perceptibly in the northeast of YRD region at 14 LST in both July and November. By comparing the land use categories of the two scenarios, we can find $PM_{2.5}$ concentration increased as LULC changed from farmland to water body. Similarly, the increase of average $PM_{2.5}$ concentration over 20 $\mu g/m^3$ occurring at 14 LST in July also corresponds to the increased area of water. Driven by gravitation, dry deposition is an important pathway to remove particulate matter from the atmosphere (Tan et al., 2020). Vegetations are efficient scavengers of $PM_{2.5}$ through interception from the atmosphere and are distinguished by higher rates of dry deposition than other land use types (Litschke and Kuttler, 2008; McDonald et al., 2007). This effect is weakened due to the decrease of vegetation cover, which leads to the increase of $PM_{2.5}$ level. Moreover, variation of $PM_{2.5}$ in different regions is related to

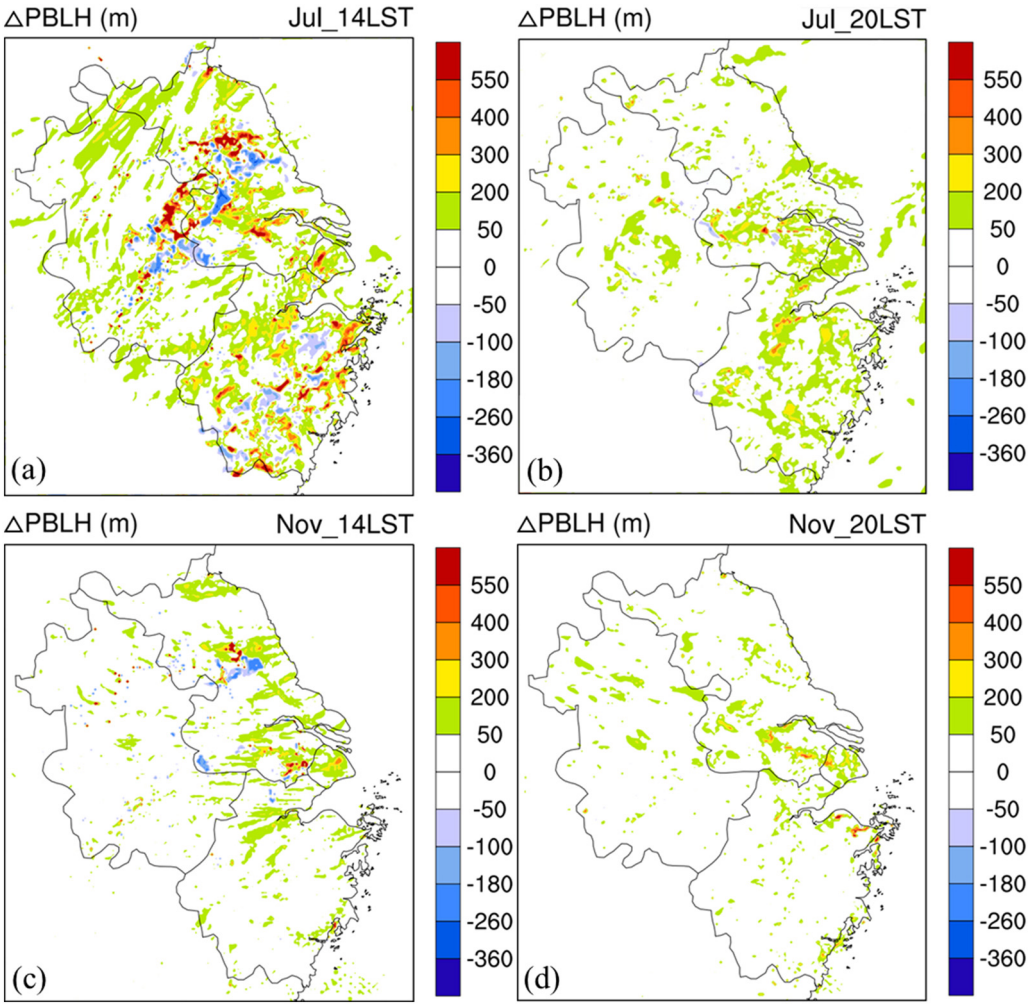


**Fig. 6.** Spatial distribution of monthly average PBLH differences between LULC_2018 and LULC_2000 for July_14LST(a), July_20LST(b), November_14LST(c) and November_20LST(d).

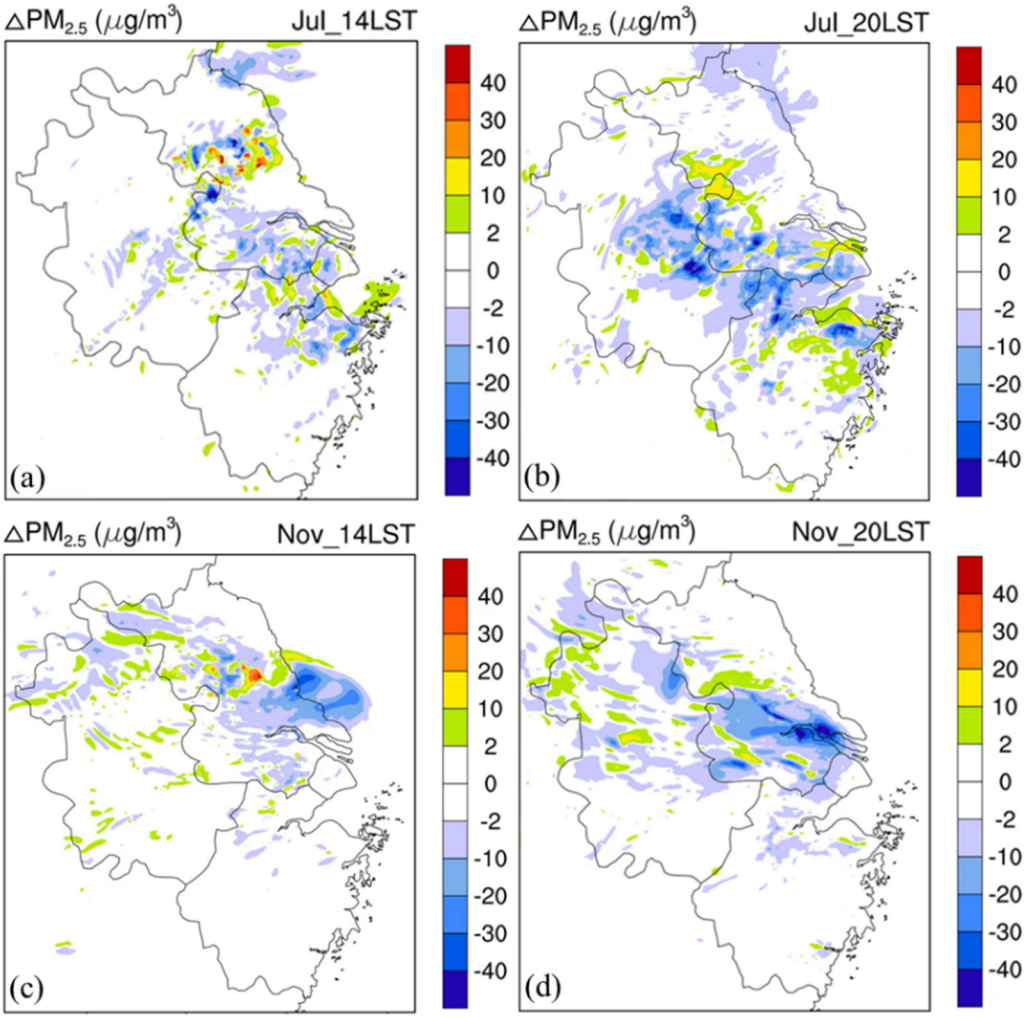


**Fig. 7.** Spatial distribution of monthly average $PM_{2.5}$ differences between LULC_2018 and LULC_2000 for July_14LST(a), July_20LST(b), November_14LST(c) and November_20LST(d).

meteorological factors, especially the changes of PBLH. Although $WS_{10}$ displays a downward trend after LULC change, the impact is offset by the increase of PBLH. PBLH can significantly influence the vertical structure of atmosphere, as most locally generated pollutants tend to be concentrated in this layer (Su et al., 2018). Except for spatial variation, $PM_{2.5}$ changes also present strong diurnal pattern. During daytime, the magnitude of decrease in $PM_{2.5}$ concentration at 14 LST in July and November are 5.4 μg/m$^3$ (~30%) and 2.2 μg/m$^3$ (~7%), respectively. During nighttime, the decreases at 20LST are larger compared to daytime, with a magnitude of 9.2 μg/m$^3$ (~38%) in July and 10.3 μg/m$^3$ (~24%) in November. During daytime, the large increase of PBLH tends to be the critical factor affecting $PM_{2.5}$ reduction. In nighttime, even though the vertical diffusion of PBLH is minimal, $PM_{2.5}$ still exhibits a notable downward transport in urban areas. Meanwhile, we find that distribution of $PM_{2.5}$ concentration with large reduction mostly corresponds to areas where wind speed shows slight decrease or even increase, which indicates that the degree of wind speed weakening exerts an influence on the change in $PM_{2.5}$ concentration at nighttime.

The chemical components of $PM_{2.5}$ (sulfate, nitrate, ammonium, elemental carbon (EC), and organic carbon (OC)) differences exhibit different spatial pattern (Figs. 8 and 9), among which nitrate decreases the most, which is mainly attributable to two reasons: first, the increasing temperature causes evaporation of nitrate; second, as the oxidation product of $NO_x$, the reduction of nitrate is related to the decrease in $NO_x$, which will be analyzed in Section 3.4.2. Sulfate shows an increasing trend especially in urban regions in summer, which is mainly due attributable to the faster oxidation of $SO_2$ caused by increasing temperature. As for OC and EC, they show an overall trend consistent to $PM_{2.5}$.

The relationships between the variation in meteorological parameters and variation in $PM_{2.5}$ concentration in SH, NJ, HZ, and HF suggest that $PM_{2.5}$ concentration is inversely correlated with $T_2$, PBLH, and $WS_{10}$ while positively correlated with RH (Fig. 10). Specifically, increases in $T_2$, PBLH, and $WS_{10}$ lead to decreases in $PM_{2.5}$ concentration, with correlation coefficient of −0.34(−0.25), −0.57(−0.40), and − 0.29(−0.38) in July (November), respectively. The influence of PBLH on $PM_{2.5}$ concentration is stronger than the influences of $T_2$ and $WS_{10}$. Despite the general decrease in wind speeds in the urban areas of YRD, $PM_{2.5}$ concentrations still show a decreasing trend due to that the transport and diffusion effect of PBLH overwhelms the accumulation effect caused by the decrease of wind speed. On the other hand, RH is positively correlated with $PM_{2.5}$ concentration with correlation coefficient of 0.47 and 0.36 in July and November. High relative humidity favors hygroscopic growth of aerosols and accelerates the transformation of gaseous pollutants into secondary aerosols components in $PM_{2.5}$ (Cheng et al., 2015; Qiao et al., 2016). Seasonally, the correlation of $T_2$ and PBLH with $PM_{2.5}$ concentration is stronger in summer than in winter while correlation of $WS_{10}$ and RH with $PM_{2.5}$ concentration is stronger in winter than in summer.

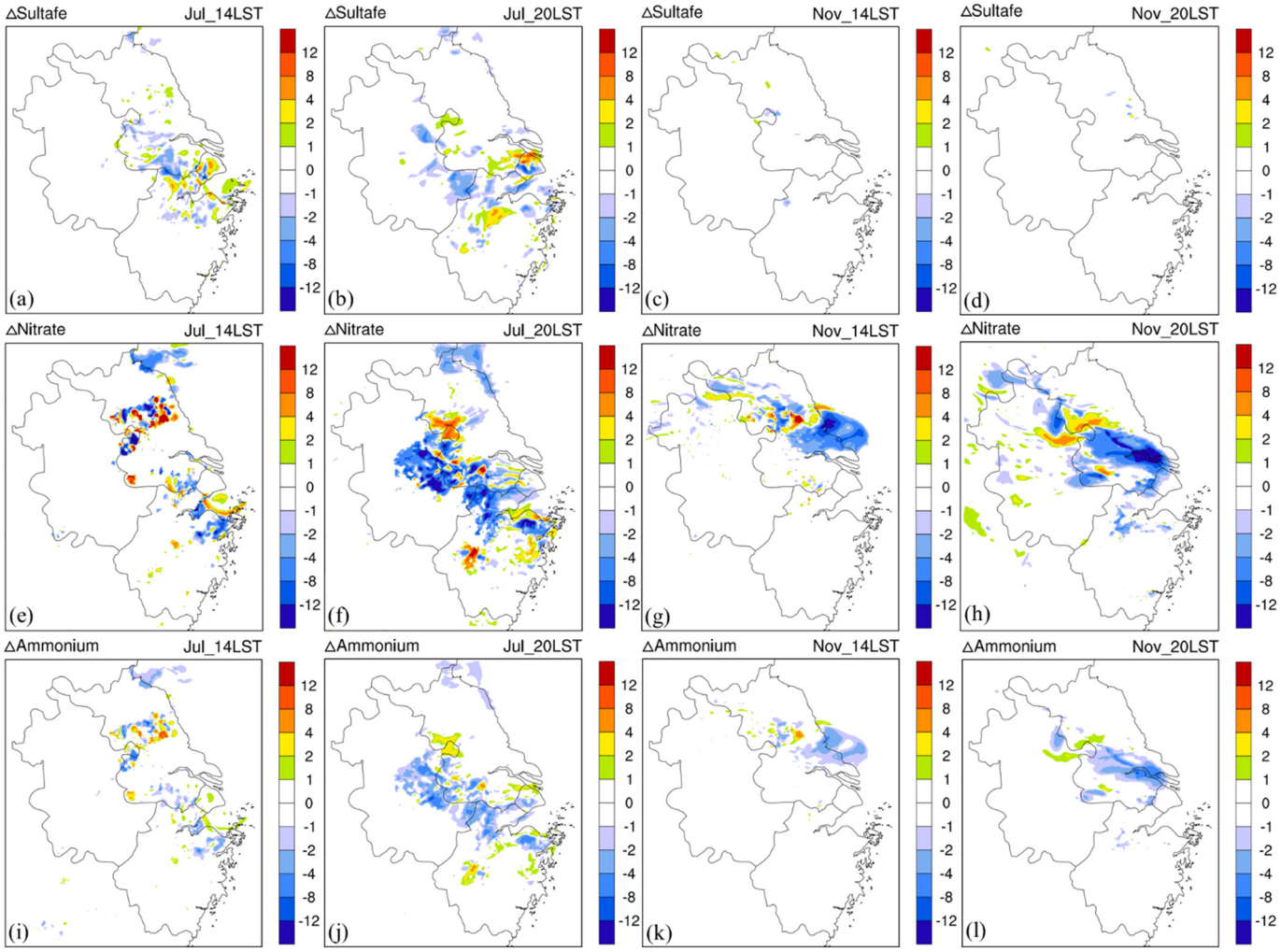


**Fig. 8.** Spatial distribution of monthly average sulfate, nitrate, and ammonium differences between LULC_2018 and LULC_2000.

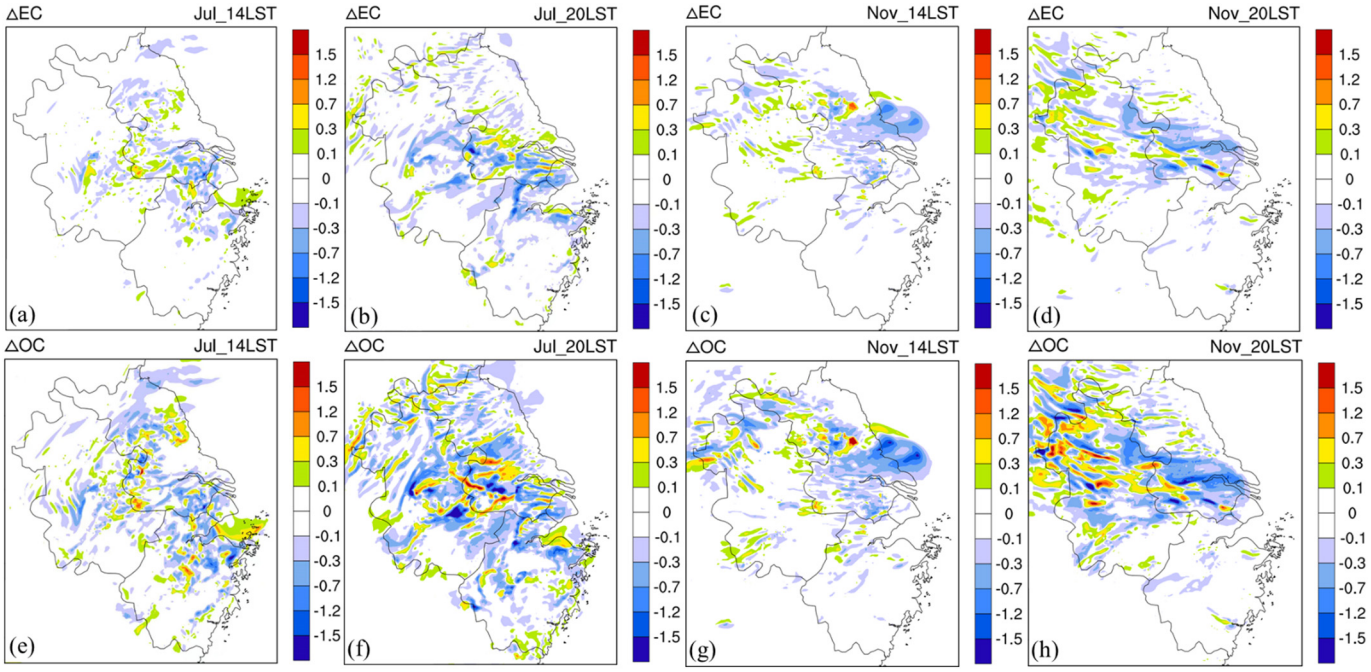


**Fig. 9.** Spatial distribution of monthly average EC and OC differences between LULC_2018 and LULC_2000.

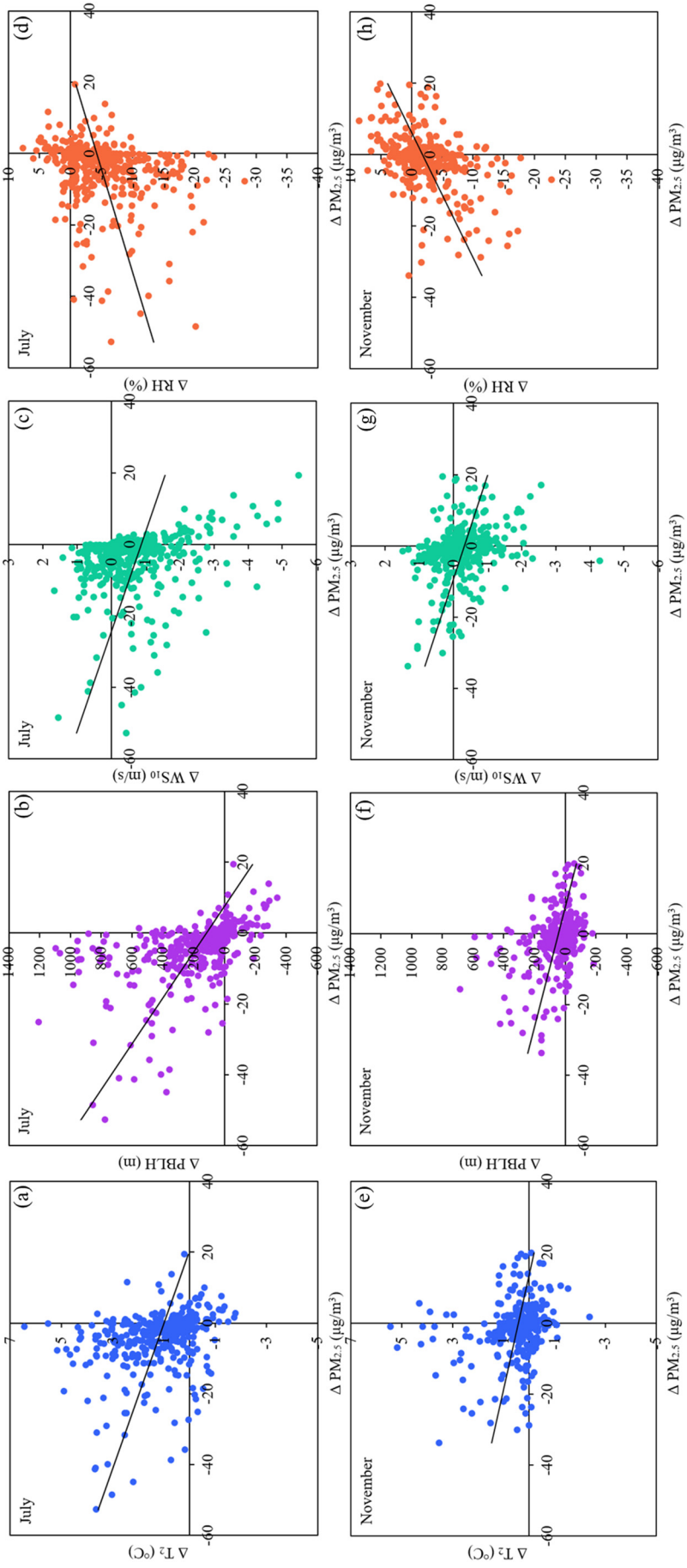


**Fig. 10.** Scatter diagrams of the relationships between the differences of meteorological parameters ($T_2$, PBLH, $WS_{10}$, and RH) and differences of $PM_{2.5}$ concentration in July (a-d) and November (e-h), respectively.

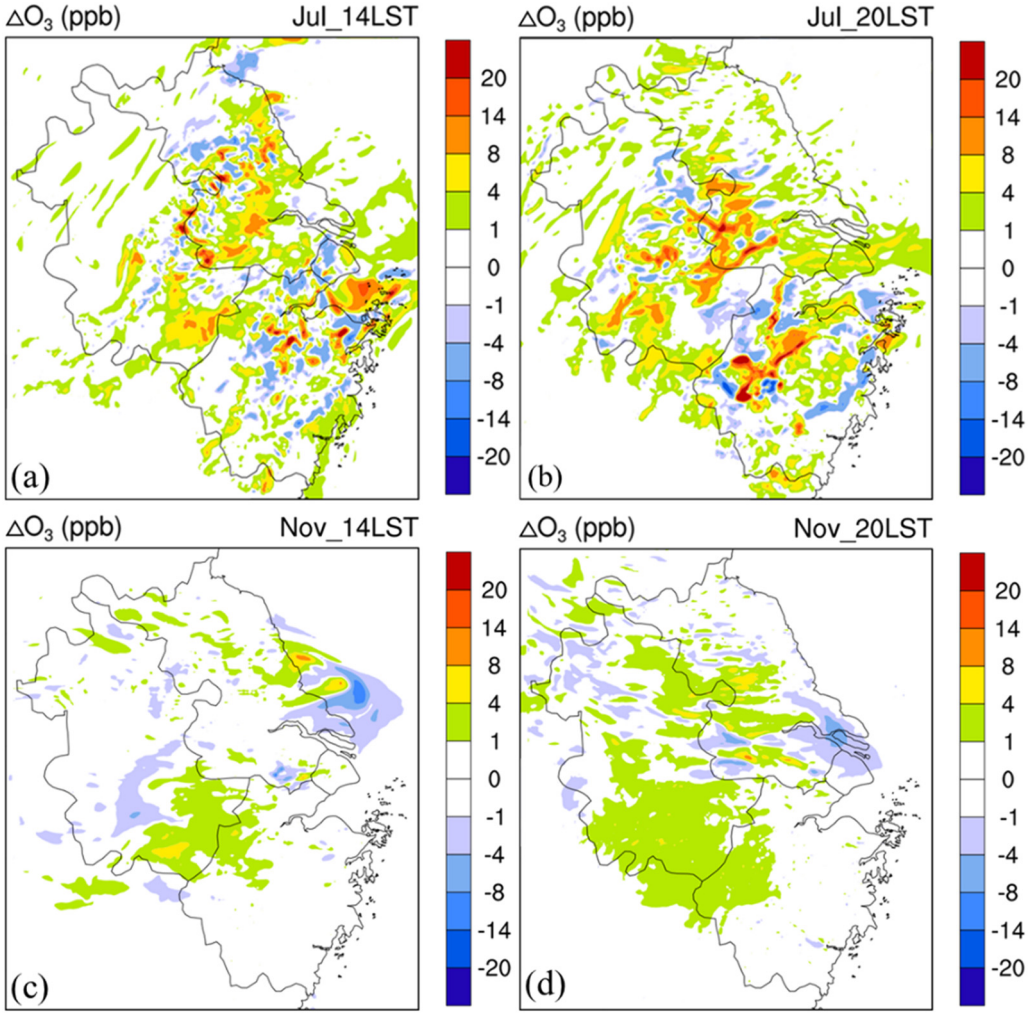


**Fig. 11.** Spatial distribution of monthly average $O_3$ differences between LULC_2018 and LULC_2000 for July_14LST(a), July_20LST(b), November_14LST(c) and November_20LST(d).

*3.4.2. $O_3$ and precursor concentrations*

In this section, the impact of surface temperature, wind speed, and PBLH changes on the formation and transport of $O_3$ are analyzed. As urbanization grows from the year 2000 to 2018, $O_3$ concentrations over urban areas increase for the whole day and exhibit a diurnal pattern (Fig. 11). The difference of $O_3$ concentration over urban areas is about 9.8 ppb (~17%) at 14 LST and 7.2 ppb (~20%) at 20 LST in July, and 1.9 ppb (~6%) at 14 LST and 2.1 ppb (~9%) at 20 LST in November respectively. Larger differences are mainly concentrated in mega-cities including SH, NJ, and HZ. Due to the mixing and transport of wind, $O_3$ level in the areas nearby the urban expanse raises at a lower rate. In addition, areas where $O_3$ concentrations rise generally coincide with the areas where wind speed decreases and temperature increases. Moreover, the decreases in RH and water vapor mixing ratio (Fig. S5) also promote the rise in $O_3$ concentrations. The changes of $O_3$ concentrations also exhibit certain seasonality that the increase of $O_3$ concentration for July is larger than November. Higher temperatures in summer promote the production of ozone by accelerating the rate of chemical reactions (Strong et al., 2013). Previous studies also show the direct relationship between higher temperatures and increased $O_3$ concentrations (Aw and Kleeman, 2003; Gupta and Mohan, 2015; Sillman and Samson, 1995).

In addition to the direct effect on $O_3$ concentration changes caused by changes of meteorological parameters, $O_3$ concentrations can also be affected by photochemistry via precursors. The oxides of nitrogen ($NO_x$) and volatile organic compounds (VOCs) play important roles in atmospheric chemistry producing $O_3$. $NO_2$ generates NO and an O atom through photolysis, and then the single O atom combines with an $O_2$ molecule to produce ozone. Furthermore, NO can react with ozone to yield $NO_2$ and $O_2$. Areas in urban with increasing $O_3$ concentrations generally coincide with the areas where $NO_x$ decrease (Fig. 12). Fig. 13 presents the diurnal variation of $O_3$ and $NO_x$ level for LULC_2000 and LULC_2018 scenarios in the urban areas of SH, NJ, HZ, and HF in July. The $O_3$ production of LULC_2018 is higher in the afternoon and nighttime, which results in higher $O_3$ level over urban areas. $O_3$ concentration increases largest during daytime in NJ by up to 7.4 ppb. The variation of $O_3$ level is inversely correlated with the variation of $NO_x$ and VOCs. The lower $NO_x$ of LULC_2018 can be attributed to the greater conversion of $NO_x$ to $O_3$ during daytime. Additionally, $NO_x$ is reduced over urban regions due to the change in PBLH and meteorological conditions. The concentrations of $NO_x$ drop as PBLH increases, which is similar to the trend of $PM_{2.5}$. Similar results are also reported by Tao et al. (2018). The decrease of $NO_x$ ranges from 1.3 to 7.5 ppb during daytime and 5.4 to 8.8 ppb during nighttime, the maxima occur in the rush hour of the evening over urban areas. Due to decrease of $NO_x$ in urban regions, the titration effect of $O_3$ is weakened, causing increase of $O_3$ concentration.

The distribution of difference for $VOC_S$ (Fig. 14) is similar to that for $NO_x$. The decrease of VOCs is mainly distributed in urban areas. The average negative differences for VOCs over urban areas are 3.7(2.2) ppb at 14LST and 10.5(7.8) ppb at 20LST in July (November), respectively. Under the condition of same anthropogenic emissions, VOCs primarily

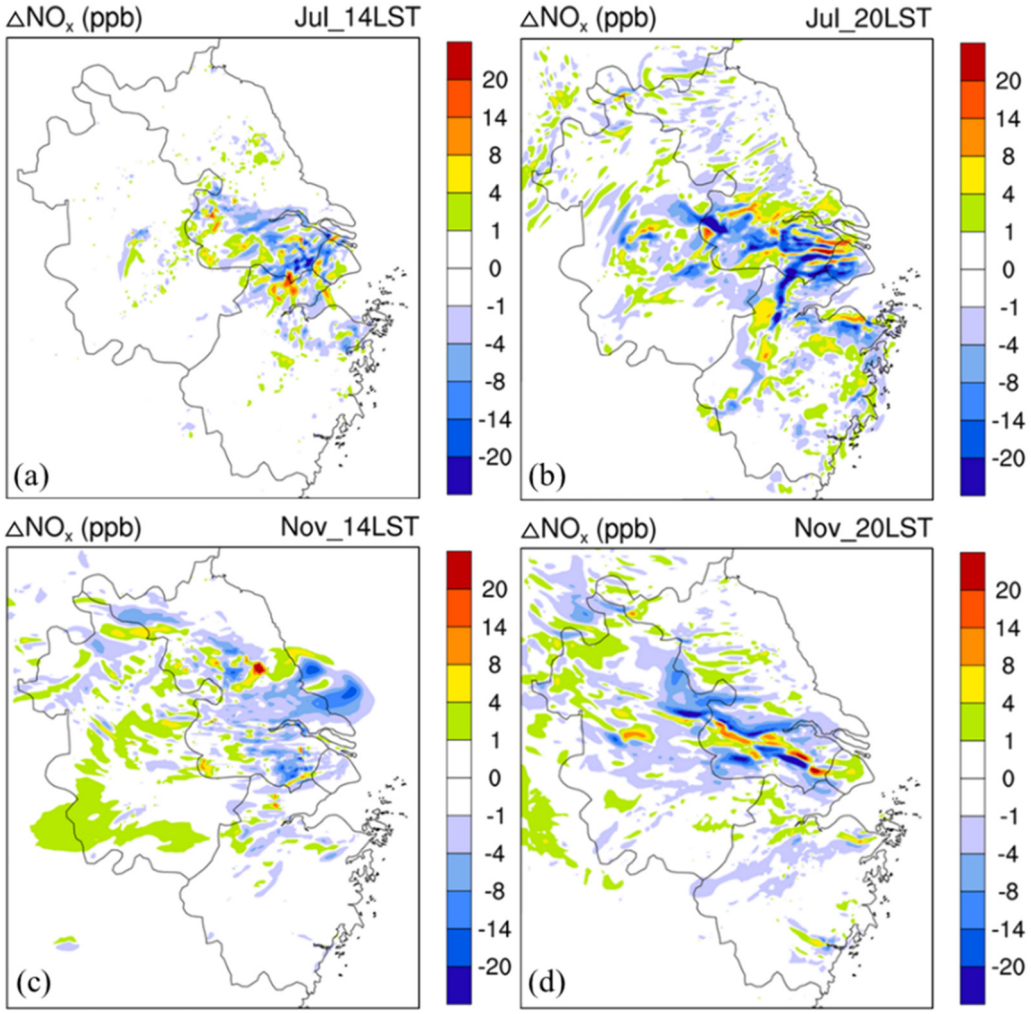


**Fig. 12.** Spatial distribution of monthly average $NO_x$ differences between LULC_2018 and LULC_2000 for July_14LST(a), July_20LST(b), November_14LST(c) and November_20LST(d).

emitted by natural vegetation exhibit reduction due to the conversion of a large amount of croplands land and forests into urban construction land. Similar change patterns of VOCs to $NO_x$ due to LULC change are also reported by Wang et al. (2009b).

### *3.5. Impacts of LULC change over various surface terrains*

The land cover of the YRD region is complex: plains are mainly distributed in the north and eastern area, while there are low and medium-high mountains as well as hills in the southern and southwest region. The eastern area is adjacent to the ocean, and most of this region is consisted of small watersheds with small catchment areas and storage capacity (Chen et al., 2020). Affected by topography and climate, the YRD region has large spatial heterogeneities. Impacts of LULC change exhibit different performances in different types of terrain (Table 4 and Table 5). The increases of $T_2$ in coastal areas are lower than those in suburban plains, while are higher than those in urban plains. It is worth noting that $T_2$ in hilly areas exhibits slight reduction during summer, leading to decreases in $O_3$ consequently. For wind speed, some hilly areas exhibit an increase at summer night. After LULC change, the stronger local circulation effect in the mountainous areas where some valleys are urban makes the increase in wind speed at night. Although the increases of PBLH in the hilly regions are larger than those in suburban plains at daytime, the decreases of $PM_{2.5}$ concentration in the hilly regions are lower. It can be attributed to the large negative differences of wind speed in hilly regions during daytime, which alleviate the diffusion of $PM_{2.5}$. In contrast to summer, the increases of $O_3$ in suburban plains and hilly areas are higher than in urban plains in winter.

## 4. Conclusions

In this study, we used the WRF/Chem modeling system coupled with detailed land use data to investigate the impacts of LULC change over nearly two decades (2000–2018) on meteorology and air quality in the rapidly-expanded city cluster, the YRD region. LULC change over YRD region during 2000–2018 presents conspicuous regional differentiation with a rapid increase in urban and built-up land area and occupied large area of croplands. The monthly average $T_2$ in urban areas increases by 1.5 °C and 0.4 °C during daytime in July and November, respectively. Positive differences of $T_2$ during nighttime are higher, as more radiation is trapped and heat released during nighttime under high-level urbanization, resulting in a rise in surface air temperature. Accordingly, RH in urban areas decreases with the increase in $T_2$ and decrease in evaporation of water. Rapid urbanization also results in changes in surface roughness, increasing the surface resistance. The deduction of $WS_{10}$ in urban areas in summer (winter) is 1.3 (0.7) m/s during daytime and 1.1 (0.5) m/s during nighttime. The decrease of wind speed in summer is significantly greater than in winter. The diurnal variations and spatial distribution changes of PBLH are similar to $T_2$. The biggest PBLH increase is found during daytime in July (289 m), while the smallest increase occurs during nighttime in November

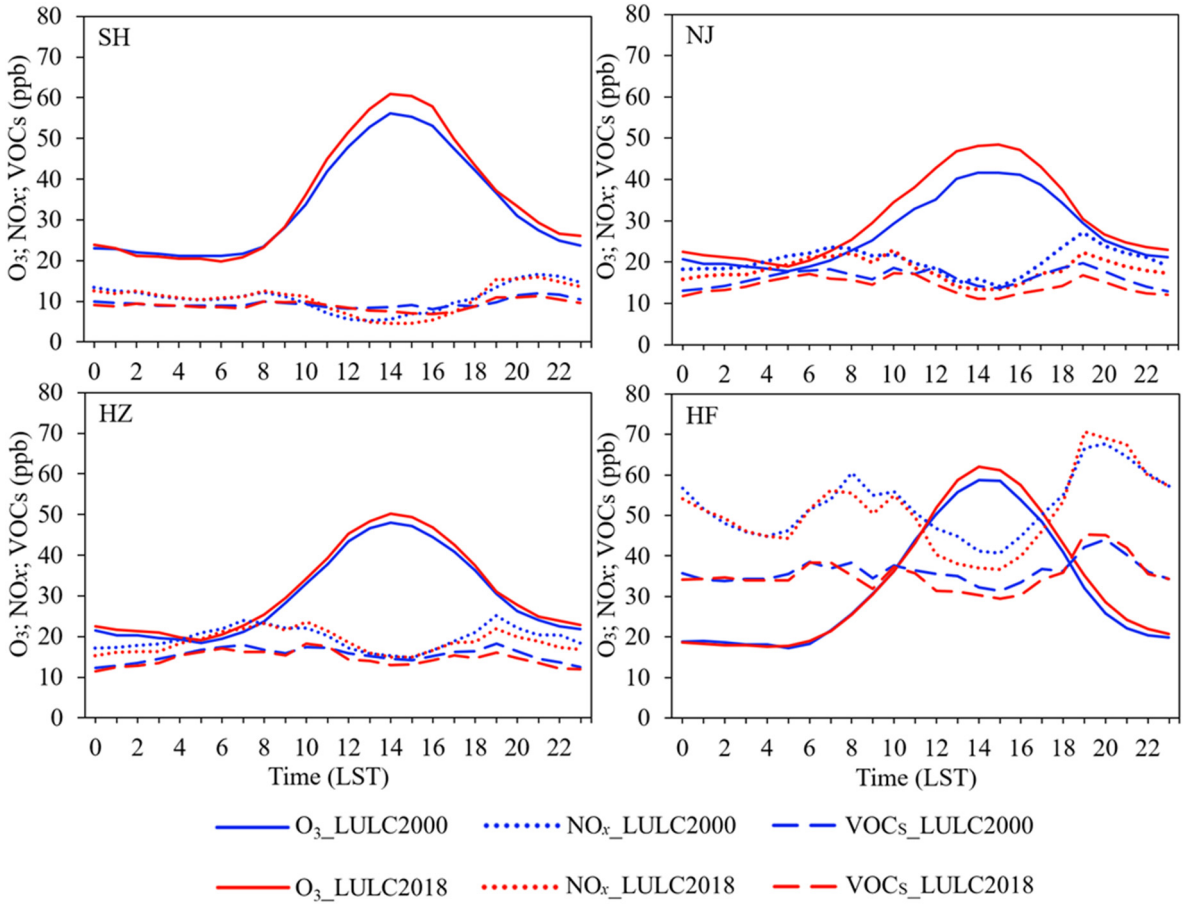


**Fig. 13.** Monthly average simulations of diurnal $O_3$, $NO_x$, and VOCs concentrations for LULC_2000 and LULC_2018 scenarios in SH, NJ, HZ, and HF during July.

(45 m). Changes in $T_2$, RH, $WS_{10}$, and PBLH mainly occur in downtown urban areas.

Spatial and temporal distributions of $PM_{2.5}$ and $O_3$ are investigated. Due to the increases of $T_2$ and PBLH, $PM_{2.5}$ level exhibits noticeable reductions in urban region with the magnitude of 5.4(2.2) μg/m$^3$ at 14LST and 9.2 (10.3) μg/m$^3$ at 20LST in summer(winter). The large increase of PBLH is found to be the crucial factor affecting $PM_{2.5}$ concentration reduction during daytime. According to spatial distribution disparities, the decrease in $PM_{2.5}$ concentration is concentrated in urban regions. Furthermore, the conversion of other land use categories to water results in an increase in $PM_{2.5}$. As for the relationships between $PM_{2.5}$ concentration and meteorological parameters, the variation of PM2.5 concentration is inversely correlated with variation of T2, PBLH, and WS10 while positively correlated with variation of RH. For impacts on $O_3$, surface $O_3$ concentrations increase obviously in July over major cities, reaching 9.8 ppb during daytime and 7.2 ppb during nighttime. In November, the changes in $O_3$ concentrations are about +1.9 ppb during daytime and + 2.1 ppb during nighttime in urban areas. Areas where $O_3$ rises are generally consistent with the areas where $WS_{10}$ decreases and $T_2$ increases, especially in summer. The inverse correlation between $O_3$ and $NO_x$ variation manifests that $NO_x$ decrease may lead to a slight increase in $O_3$ concentration in urban regions. The reduction in $NO_x$ during nighttime is greater than that during nighttime in summer, resulting in a larger positive difference of $O_3$ concentration during nighttime in summer. Regarding different terrains, impacts of LULC changes are dissimilar. $O_3$ level decreases in hilly areas during summer due to slight reduction in $T_2$. For winter, the increases of $O_3$ concentration in suburban plains and hilly areas are higher than in urban plains.

In addition to the effects discussed in this paper, LULC change also involves several dynamic and thermal effects such as drag effect, urban heat island effect, anthropogenic heat effect, and shading effect. Integrating surface parameters such as leaf area index, green vegetation fraction, and urban canopy height may help to better understand the effects of urbanization on climate and air quality. Future work will be conducted to further explore the association between urban surface changes and regional air quality.

## CRediT authorship contribution statement

L. Li designed and led the research. A. S. Zhu and L. Li prepared the paper with contributions from all co-authors. Q. Wang and M. Wang conducted satellite data processing. A.S. Zhu, L. Huang, Y.J. Wang performed modeling work. L. Li and A. Chan reviewed the paper.

## Declaration of competing interest

The authors declare that they have no conflict of interest.

## Acknowledgement

This study was financially supported by the National Natural Science Foundation of China (No. 42075144, No. 42005112), and the Shanghai International Science and Technology Cooperation Fund (No. 19230742500).

## Appendix A. Supplementary data

Supplementary data to this article can be found online at https://doi.org/10.1016/j.scitotenv.2022.154669.

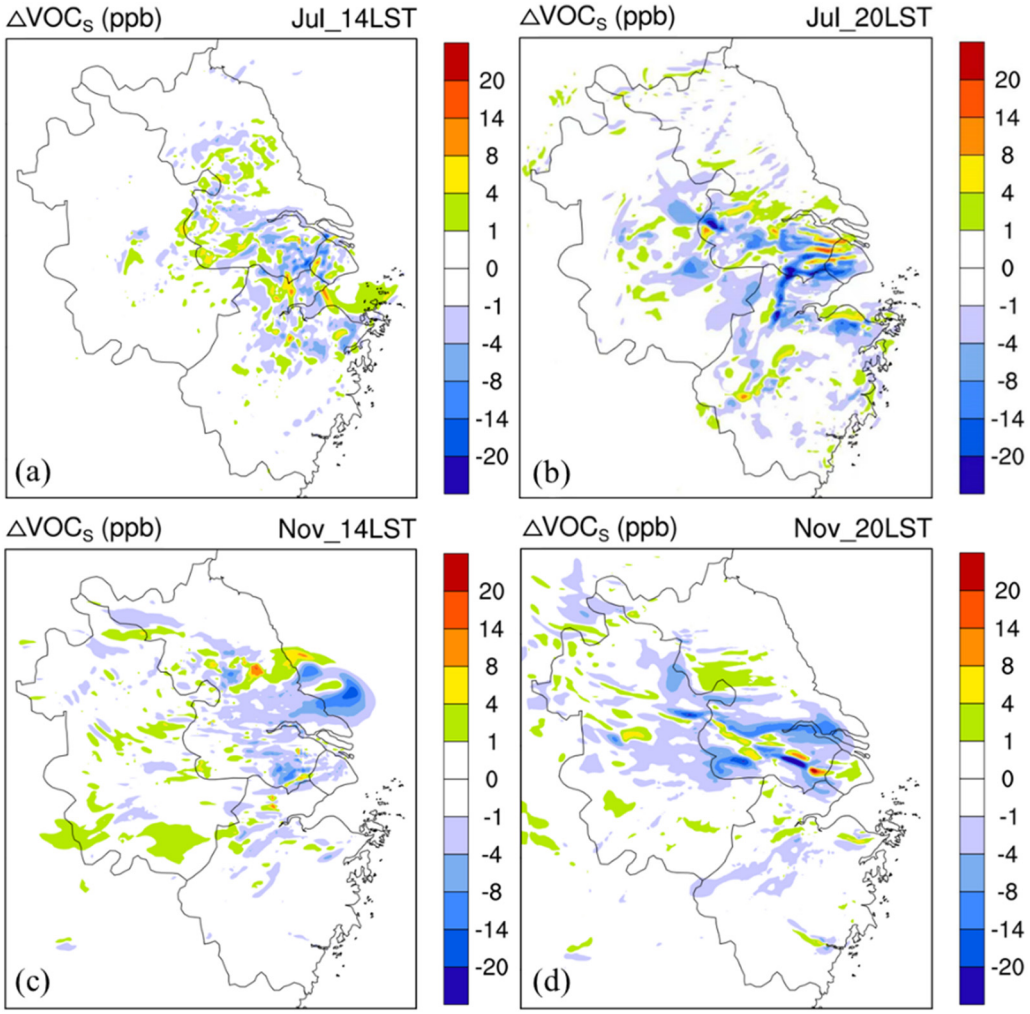


**Fig. 14.** Spatial distribution of monthly average $VOC_S$ differences between LULC_2018 and LULC_2000 for July_14LST(a), July_20LST(b), November_14LST(c) and November_20LST(d).

**Table 4**
Simulated differences of meteorological variables and air pollutants at typical stations in various terrain types during daytime (nighttime) in summer.

| Terrain | Stations | $\Delta T_2$(°C) | $\Delta WS_{10}$(m/s) | ΔRH(%) | ΔPBLH(m) | $\Delta PM_{2.5}$(μg/m$^3$) | $\Delta O_3$(ppb) |
|---|---|---|---|---|---|---|---|
| Plain(urban) | Shanghai | 1.4(2.8) | −1.0(−1.4) | −11(−3) | 336(167) | −3.8(−10.5) | 5.4(3.1) |
| | Nanjing | 0.7(1.8) | −1.1(−2.4) | −3(−4) | 288(125) | −5.1(−12.9) | 9.5(8.4) |
| | Hangzhou | 1.1(2.0) | −0.8(−1.6) | −8(−9) | 131(84) | −4.2(−11.4) | 3.1(1.2) |
| | Hefei | 0.8(2.1) | −0.5(−1.9) | −2(−17) | 125(77) | −8.2(−15.7) | 6.5(7.5) |
| | **Avg.** | **1.0(2.2)** | **−0.9(−1.8)** | **−6(−8)** | **220(113)** | **−5.3(−12.6)** | **6.1(5.1)** |
| Plain(suburban) | Bozhou | 0.3(0.9) | −0.1(−0.4) | −1(−6) | 63(48) | −0.5(−0.7) | 0.3(0.2) |
| | Xuzhou | 0.1(0.6) | −0.5(−0.8) | −2(−7) | 78(51) | −1.2(−4.2) | 2.3(0.4) |
| | Wuhu | 0.4(0.7) | −0.4(−0.5) | −2(−4) | 32(11) | −7.2(−11.1) | −0.2(3.4) |
| | Shengzhou | −0.4(0.2) | −0.6(−0.2) | 3(2) | 14(58) | −3.5(2.1) | 1.6(1.2) |
| | **Avg.** | **0.1(0.6)** | **−0.4(−0.5)** | **1(−4)** | **47(42)** | **−3.1(−4.5)** | **1.0(1.3)** |
| Coastal | Ganyu | 1.2(0.4) | −0.4(−1.3) | −13(−11) | 311(77) | −7.5(−6.5) | 1.2(0.5) |
| | Shipu | 1.1(0.5) | −1.8(−2.5) | −1(−2) | 289(55) | −2.1(−3.8) | 0.4(0.5) |
| | Zhoushan | 0.9(0.8) | −0.3(−2.7) | −3(−2) | 214(22) | −5.4(−7.7) | 2.5(1.3) |
| | Dongtai | 0.1(0.3) | −0.9(−2.4) | −1(−4) | 114(5) | −1.4(−1.8) | 0.8(0.4) |
| | **Avg.** | **0.8(0.5)** | **−0.9(−2.2)** | **−5(−5)** | **232(40)** | **−4.1(−4.9)** | **1.2(0.7)** |
| Hilly | Huangshan | −0.4(−0.5) | −0.7(−0.6) | 7(3) | 152(31) | −0.2(−0.1) | 1.5(−0.8) |
| | Jinyun | −0.1(0.3) | −1.8(0.3) | 9(5) | 259(50) | −0.3(−0.5) | −1.3(−1.5) |
| | Xianju | −0.3(−0.2) | −2.2(0.4) | 13(7) | 314(48) | −0.5(0.2) | −3.3(−4.8) |
| | Huoshan | −0.5(−0.6) | −0.6(−0.4) | 3(5) | 56(22) | −0.8(−1.1) | −0.5(−1.2) |
| | **Avg.** | **−0.3(−0.3)** | **−1.3(−0.1)** | **8(5)** | **195(38)** | **−0.5(−0.5)** | **−1.0(−2.1)** |

**Table 5**
Simulated differences of meteorological and air pollutants at typical stations in various terrain types during daytime (nighttime) in winter.

| Terrain | Stations | $\Delta T_2$(°C) | $\Delta WS_{10}$(m/s) | ΔRH(%) | ΔPBLH(m) | $\Delta PM_{2.5}$(μg/m$^3$) | $\Delta O_3$(ppb) |
|---|---|---|---|---|---|---|---|
| Plain(urban) | Shanghai | 0.9(2.1) | −0.8(−0.6) | −4(−14) | 256(135) | −0.5(−4.5) | 0.5(−1.8) |
| | Nanjing | 0.2(0.9) | −0.6(−1.1) | −1(−13) | 63(23) | −1.8(−9.1) | 0.8(1.7) |
| | Hangzhou | 0.3(1.2) | −0.1(−0.3) | −7(−9) | 77(54) | −3.5(−7.7) | 0.5(0.2) |
| | Hefei | 0.1(0.4) | −0.9(−1.2) | −3(−10) | 68(49) | −4.9(−13.5) | 0.4(2.2) |
| | **Avg.** | **0.4(1.2)** | **−0.6(−0.8)** | **−4(−12)** | **116(65)** | **−2.7(−8.7)** | **0.6(0.6)** |
| Plain(suburban) | Bozhou | 0.2(0.5) | −0.4(−0.4) | −1(−4) | 67(51) | −1.2(−11.3) | 0.8(2.2) |
| | Xuzhou | 0.3(0.7) | −0.3(−0.7) | 0(−6) | 72(69) | −3.4(−5.1) | 3.4(2.8) |
| | Wuhu | 0.1(0.5) | −0.2(−0.6) | −3(−2) | 23(11) | −0.2(−3.8) | 3.9(−1.1) |
| | Shengzhou | 0.2(0.6) | −0.1(−0.1) | −2(−4) | 42(15) | −0.6(−1.5) | 0.5(1.0) |
| | **Avg.** | **0.2(0.6)** | **−0.3(−0.5)** | **−2(−4)** | **51(37)** | **−1.4(−5.4)** | **2.2(1.2)** |
| Coastal | Ganyu | 0.4(0.5) | −0.9(−0.8) | −7(−4) | 114(39) | 0.4(−1.5) | 0.3(0.5) |
| | Shipu | 0.1(0.3) | −0.3(−0.4) | 0(2) | 79(58) | −0.6(−0.8) | 0.2(0.1) |
| | Zhoushan | 0.2(0.2) | −0.1(−0.3) | −1(−2) | 33(19) | 0.3(−0.1) | 0.8(0.4) |
| | Dongtai | 0.1(0.2) | −0.1(−0.1) | −3(−3) | 47(25) | −0.6(−1.1) | −1.2(−0.9) |
| | **Avg.** | **0.2(0.3)** | **−0.4(−0.4)** | **−3(−2)** | **68(30)** | **−0.5(−0.9)** | **0.0(0.1)** |
| Hilly | Huangshan | −0.1(0.2) | 0.0(−0.1) | 2(−1) | 21(14) | −0.1(−1.4) | 4.2(3.4) |
| | Jinyun | 0.4(0.6) | −0.2(−0.4) | −4(−2) | 18(6) | 0.2(−0.3) | 0.8(1.2) |
| | Xianju | 0.2(0.1) | −0.1(−0.1) | −2(−3) | 44(14) | −0.6(−0.1) | 0.9(0.5) |
| | Huoshan | 0.1(0.7) | 0.0(−0.2) | −1(−2) | 15(11) | −1.1(−3.6) | 0.7(1.9) |
| | **Avg.** | **0.2(0.4)** | **−0.1(−0.2)** | **−1(−2)** | **25(11)** | **−0.4(−1.4)** | **1.7(1.8)** |

## References


Aw, J., Kleeman, M.J., 2003. Evaluating the first-order effect of intraannual temperature variability on urban air pollution. J. Geophys. Res. Atmos. 108.

Ayotte, K.W., Sullivan, P.P., Andren, A., Doney, S.C., Holtslag, A.A., Large, W.G., et al., 1996. An evaluation of neutral and convective planetary boundary-layer parameterizations relative to large eddy simulations. Bound.-Layer Meteorol. 79, 131–175.

Boylan, J.W., Russell, A.G., 2006. PM and light extinction model performance metrics, goals, and criteria for three-dimensional air quality models. Atmos. Environ. 40, 4946–4959.

Chen, F., Dudhia, J., 2001. Coupling an advanced land surface–hydrology model with the Penn State–NCAR MM5 modeling system. Part I: model implementation and sensitivity. Mon. Weather Rev. 129, 569–585.

Chen, L., Zhang, M., Zhu, J., Wang, Y., Skorokhod, A., 2018. Modeling impacts of urbanization and urban heat island mitigation on boundary layer meteorology and air quality in Beijing under different weather conditions. J. Geophys. Res. Atmos. 123, 4323–4344.

Chen, J., Li, Q., Wang, H., Deng, M., 2020. A machine learning ensemble approach based on random forest and radial basis function neural network for risk evaluation of regional flood disaster: a case study of the Yangtze River Delta, China. Int. J. Environ. Res. Public Health 17, 49.

Cheng, F.Y., Byun, D.W., 2008. Application of high resolution land use and land cover data for atmospheric modeling in the Houston-Galveston metropolitan area, part I: meteorological simulation results. Atmos. Environ. 42, 7795–7811.

Cheng, Y., He, K.B., Du, Z.Y., Zheng, M., Duan, F.K., Ma, Y.L., 2015. Humidity plays an important role in the PM2.5 pollution in Beijing. Environ. Pollut. 197, 68–75.

Cole, M.A., Neumayer, E., 2004. Examining the impact of demographic factors on air pollution. Popul. Environ. 26, 5–21.

Deng, Y., Qi, W., Fu, B., Wang, K., 2020. Geographical transformations of urban sprawl: exploring the spatial heterogeneity across cities in China 1992–2015. Cities 105, 102415.

Dewan, A.M., Yamaguchi, Y., Rahman, M.Z., 2012. Dynamics of land use/cover changes and the analysis of landscape fragmentation in Dhaka Metropolitan, Bangladesh. GeoJournal 77, 315–330.

Du, Y., Xie, Z., Zeng, Y., Shi, Y., Wu, J., 2007. Impact of urban expansion on regional temperature change in the Yangtze River Delta. J. Geogr. Sci. 17, 387–398.

El-Hamid, H.T.A., Caiyong, W., Yongting, Z., 2021. Geospatial analysis of land use driving force in coal mining area: case study in Ningdong, China. GeoJournal 86, 605–620.

Emery, C., Tai, E., Yarwood, G., 2001. Enhanced meteorological modeling and performance evaluation for two Texas ozone episodes. Prepared for the Texas Natural Resource Conservation Commission, by ENVIRON International Corporation.

Epa, U., 2007. Guidance on the use of models and other analyses for demonstrating attainment of air quality goals for ozone, PM2. 5, and regional haze. US Environmental Protection Agency, Office of Air Quality Planning.

Fang, C., Liu, H., Li, G., Sun, D., Miao, Z., 2015. Estimating the impact of urbanization on air quality in China using spatial regression models. Sustainability 7, 15570–15592.

Ghimire, B., Williams, C.A., Masek, J., Gao, F., Wang, Z., Schaaf, C., et al., 2014. Global albedo change and radiative cooling from anthropogenic land cover change, 1700 to 2005 based on MODIS, land use harmonization, radiative kernels, and reanalysis. Geophys. Res. Lett. 41, 9087–9096.

Gong, P., Li, X., Zhang, W., 2019. 40-year (1978–2017) human settlement changes in China reflected by impervious surfaces from satellite remote sensing. Science Bulletin 64, 756–763.

Grell, G.A., Peckham, S.E., Schmitz, R., McKeen, S.A., Frost, G., Skamarock, W.C., et al., 2005. Fully coupled "online" chemistry within the WRF model. Atmos. Environ. 39, 6957–6975.

Gu, C., Hu, L., Zhang, X., Wang, X., Guo, J., 2011. Climate change and urbanization in the Yangtze River Delta. Habit. Int. 35, 544–552.

Guenther, A., Karl, T., Harley, P., Wiedinmyer, C., Palmer, P.I., Geron, C., 2006. Estimates of global terrestrial isoprene emissions using MEGAN (Model of emissions of gases and aerosols from Nature). Atmos. Chem. Phys. 6, 3181–3210.

Güneralp, B., Perlstein, A.S., Seto, K.C., 2015. Balancing urban growth and ecological conservation: a challenge for planning and governance in China. Ambio 44, 532–543.

Gupta, M., Mohan, M., 2015. Validation of WRF/Chem model and sensitivity of chemical mechanisms to ozone simulation over megacity Delhi. Atmos. Environ. 122, 220–229.

Haeffelin, M., Angelini, F., Morille, Y., Martucci, G., Frey, S., Gobbi, G., et al., 2012. Evaluation of mixing-height retrievals from automatic profiling lidars and ceilometers in view of future integrated networks in Europe. Bound.-Layer Meteorol. 143, 49–75.

Han, J., Meng, X., Zhou, X., Yi, B., Liu, M., Xiang, W.-N., 2017. A long-term analysis of urbanization process, landscape change, and carbon sources and sinks: a case study in China's Yangtze River Delta region. J. Clean. Prod. 141, 1040–1050.

Hong, S.-Y., Noh, Y., Dudhia, J., 2006. A new vertical diffusion package with an explicit treatment of entrainment processes. Mon. Weather Rev. 134, 2318–2341.

Huang, L., Zhu, Y.H., Zhai, H.H., Xue, S.H., Zhu, T.Y., Shao, Y., Liu, Z.Y., Emery, C., Yarwood, G., Wang, Y.J., Fu, J.S., Zhang, K., Li, L., 2021. Recommendations on benchmarks for numerical air quality model applications in China – part 1: PM2.5 and chemical species. Atmos. Chem.Phys. 21, 2725–2743.

Jia, W., Zhang, X., 2020. The role of the planetary boundary layer parameterization schemes on the meteorological and aerosol pollution simulations: a review. Atmos. Res. 239, 104890.

Kain, J.S., Fritsch, J.M., 1993. Convective parameterization for mesoscale models: the Kain-Fritsch scheme. The Representation of Cumulus Convection in Numerical Models. Springer, pp. 165–170.

Kaplan, S., Georgescu, M., Alfasi, N., Kloog, I., 2017. Impact of future urbanization on a hot summer: a case study of Israel. Theor. Appl. Climatol. 128, 325–341.

Ku, C.-A., 2020. Exploring the spatial and temporal relationship between air quality and urban land-use patterns based on an integrated method. Sustainability 12, 2964.

Li, G., Li, F., 2019. Urban sprawl in China: differences and socioeconomic drivers. Sci. Total Environ. 673, 367–377.

Li, L., An, J., Zhou, M., Qiao, L., Zhu, S., Yan, R., et al., 2018. An integrated source apportionment methodology and its application over the Yangtze River Delta region, China. Environ. Sci. Technol. 52, 14216–14227.

Li, L., An, J., Huang, L., Yan, R., Huang, C., Yarwood, G., 2019a. Ozone source apportionment over the Yangtze River Delta region, China: investigation of regional transport, sectoral contributions and seasonal differences. Atmos. Environ. 202, 269–280.

Li, L., Zhu, S., An, J., Zhou, M., Wang, H., Yan, R., et al., 2019b. Evaluation of the effect of regional joint-control measures on changing photochemical transformation: a comprehensive study of the optimization scenario analysis. Atmos. Chem. Phys. 19, 9037–9060.

Liao, J., Wang, T., Jiang, Z., Zhuang, B., Xie, M., Yin, C., et al., 2015. WRF/Chem modeling of the impacts of urban expansion on regional climate and air pollutants in Yangtze River Delta, China. Atmos. Environ. 106, 204–214.

Lin, Y.-L., Farley, R.D., Orville, H.D., 1983. Bulk parameterization of the snow field in a cloud model. J. Clim. Appl. Meteor. 22, 1065–1092.

Lin, W., Zhang, L., Du, D., Yang, L., Lin, H., Zhang, Y., et al., 2009. Quantification of land use/land cover changes in Pearl River Delta and its impact on regional climate in summer using numerical modeling. Reg. Environ. Chang. 9, 75–82.

Litschke, T., Kuttler, W., 2008. On the reduction of urban particle concentration by vegetation-a review. Meteorol. Z. 17, 229–240.

Mao, X., Wang, L., Pan, X., Zhang, M., Wu, X., Zhang, W., 2022. A study on the dynamic spatial spillover effect of urban form on PM2. 5 concentration at county scale in China. Atmos. Res. 106046.

McDonald, A., Bealey, W., Fowler, D., Dragosits, U., Skiba, U., Smith, R., et al., 2007. Quantifying the effect of urban tree planting on concentrations and depositions of PM10 in two UK conurbations. Atmos. Environ. 41, 8455–8467.

Miao, Y., Li, J., Miao, S., Che, H., Wang, Y., Zhang, X., et al., 2019. Interaction between planetary boundary layer and PM 2.5 pollution in megacities in China: a review. Curr.Pollut. Rep. 5, 261–271.
Mlawer, E.J., Taubman, S.J., Brown, P.D., Iacono, M.J., Clough, S.A., 1997. Radiative transfer for inhomogeneous atmospheres: RRTM, a validated correlated-k model for the longwave. J. Geophys. Res. Atmos. 102, 16663–16682.
Pan, J., Gu, Y., 2016. Cruise observation and numerical modeling of turbulent mixing in the Pearl River estuary in summer. Cont. Shelf Res. 120, 122–138.
Prasad, K.H., Srinivas, C., Rao, T.N., Naidu, C., Baskaran, R., 2017. Performance of WRF in simulating terrain induced flows and atmospheric boundary layer characteristics over the tropical station Gadanki. Atmos. Res. 185, 101–117.
Qiao, T., Zhao, M., Xiu, G., Yu, J., 2016. Simultaneous monitoring and compositions analysis of PM1 and PM2.5 in Shanghai: implications for characterization of haze pollution and source apportionment. Sci. Total Environ. 557, 386–394.
Ryu, Y.-H., Baik, J.-J., Kwak, K.-H., Kim, S., Moon, N., 2013. Impacts of urban land-surface forcing on ozone air quality in the Seoul metropolitan area. Atmos. Chem. Phys. 13, 2177–2194.
Sati, A.P., Mohan, M., 2018. The impact of urbanization during half a century on surface meteorology based on WRF model simulations over National Capital Region, India. Theor. Appl. Climatol. 134, 309–323.
Schell, B., Ackermann, I.J., Hass, H., Binkowski, F.S., Ebel, A., 2001. Modeling the formation of secondary organic aerosol within a comprehensive air quality model system. J. Geophys.Res. Atmos. 106, 28275–28293.
Seto, K.C., Shepherd, J.M., 2009. Global urban land-use trends and climate impacts. Curr. Opin. Environ. Sustain. 1, 89–95.
Seto, K.C., Woodcock, C., Song, C., Huang, X., Lu, J., Kaufmann, R., 2002. Monitoring land-use change in the Pearl River Delta using Landsat TM. Int. J. Remote Sens. 23, 1985–2004.
Sillman, S., Samson, P.J., 1995. Impact of temperature on oxidant photochemistry in urban, polluted rural and remote environments. J. Geophys. Res. 100, 11497–11508.
Stockwell, W.R., Middleton, P., Chang, J.S., Tang, X., 1990. The second generation regional acid deposition model chemical mechanism for regional air quality modeling. J. Geophys. Res. Atmos. 95, 16343–16367.
Strong, J., Whyatt, J.D., Metcalfe, S.E., Derwent, R.G., Hewitt, C.N., 2013. Investigating the impacts of anthropogenic and biogenic VOC emissions and elevated temperatures during the 2003 ozone episode in the UK. Atmos. Environ. 74, 393–401.
Su, T., Li, Z., Kahn, R., 2018. Relationships between the planetary boundary layer height and surface pollutants derived from Lidar observations over China: regional pattern and influencing factors. Atmos. Chem. Phys. 18, 15921–15935.
Sun, Q., Wu, Z., Tan, J., 2012. The relationship between land surface temperature and land use/land cover in Guangzhou, China. Environ. Earth Sci. 65, 1687–1694.
Tan, J., Fu, J.S., Carmichael, G.R., Itahashi, S., Tao, Z., Huang, K., et al., 2020. Why do models perform differently on particulate matter over East Asia? A multi-model intercomparison study for MICS-Asia III. Atmos. Chem. Phys. 20, 7393–7410.
Tao, H., Jia, X., Zhou, H., Xing, C., Li, G., Chen, L., et al., 2018. Impacts of land use and land cover change on regional meteorology and air quality over the Beijing-Tianjin-Hebei region, China. Atmos. Environ. 189, 9–21.
Trlica, A., Hutyra, L., Schaaf, C., Erb, A., Wang, J., 2017. Albedo, land cover, and daytime surface temperature variation across an urbanized landscape. Earth's Future 5, 1084–1101.
Vahmani, P., Sun, F., Hall, A., Ban-Weiss, G., 2016. Investigating the climate impacts of urbanization and the potential for cool roofs to counter future climate change in Southern California. Environ. Res. Lett. 11, 124027.
Verburg, P.H., de Nijs, T.C., van Eck, J.R., Visser, H., de Jong, K., 2004. A method to analyse neighbourhood characteristics of land use patterns. Comput. Environ. Urban Syst. 28, 667–690.
Wang, X., Chen, F., Wu, Z., Zhang, M., Tewari, M., Guenther, A., et al., 2009a. Impacts of weather conditions modified by urban expansion on surface ozone: comparison between the Pearl River Delta and Yangtze River Delta regions. Adv. Atmos. Sci. 26, 962–972.
Wang, X., Wu, Z., Liang, G., 2009b. WRF/CHEM modeling of impacts of weather conditions modified by urban expansion on secondary organic aerosol formation over pearl river delta. Particuology 7, 384–391.
Wang, X., Liao, J., Zhang, J., Shen, C., Chen, W., Xia, B., et al., 2014. A numeric study of regional climate change induced by urban expansion in the Pearl River, Delta. China. J. Appl. Meteorol. Climatol. 53, 346–362.
Xu, T., Ma, T., Zhou, C., Zhou, Y., 2014. Characterizing spatio-temporal dynamics of urbanization in China using time series of DMSP/OLS night light data. Remote Sens. 6, 7708–7731.
Zhan, C., Xie, M., 2022. Land use and anthropogenic heat modulate ozone by meteorology: a perspective from the Yangtze River Delta region. Atmos. Chem. Phys. 22, 1351–1371.
Zhang, H., Wang, Y., Hu, J., Ying, Q., Hu, X.-M., 2015. Relationships between meteorological parameters and criteria air pollutants in three megacities in China. Environ. Res. 140, 242–254.
Zhang, T., Zang, L., Wan, Y., Wang, W., Zhang, Y., 2019. Ground-level PM2. 5 estimation over urban agglomerations in China with high spatiotemporal resolution based on Himawari-8. Sci. Total Environ. 676, 535–544.
Zhao, P., Dong, F., Yang, Y., He, D., Zhao, X., Zhang, W., et al., 2013. Characteristics of carbonaceous aerosol in the region of Beijing Tianjin, and Hebei, China. Atmos. Environ. 71, 389–398.
Zheng, S., Zhou, X., Singh, R.P., Wu, Y., Ye, Y., Wu, C., 2017. The spatiotemporal distribution of air pollutants and their relationship with land-use patterns in Hangzhou city, China. Atmosphere 8, 110.
Zheng, B., Tong, D., Li, M., Liu, F., Hong, C., Geng, G., et al., 2018. Trends in China's anthropogenic emissions since 2010 as the consequence of clean air actions. Atmos. Chem. Phys. 18, 14095–14111.